Universiteit Utrecht

Azimuthal angular correlations between heavy-flavour electrons and charged hadrons in semi-central lead-lead collisions at 2.76 TeV at ALICE

Naghmeh Mohammadi
July 31, 2013

Master Thesis
Report number: UU(SAP) 13-8
Supervisors: Dr. Andre Mischke, Drs. Deepa Thomas
Utrecht University
Faculty of Science/Department of Physics and Astronomy
Institute for Subatomic Physics
Buys Ballot laboratory
PO BOX 80 000, 3508 TA Utrecht, The Netherlands

Abstract

The azimuthal angular correlation between heavy-flavour decay electrons and charged hadrons was measured in semi-central Pb-Pb collisions at $\sqrt{s_{\rm NN}} = 2.76$ TeV for semi-central (20-50%) events. The analysis is done by using the data samples collected with semi-central (20-50%) trigger. The ALICE Time Projection Chamber (TPC) and Electromagentic Calorimeter (EMCal) were used for electron identification. The non-heavy flavour electron background was removed by using the invariant mass method.

The near-side ($-\pi/2 < \Delta\phi < \pi/2$) yield is measured in this analysis by fitting a Gaussian and the flow function on the near-side. The near-side yield from this centrality selection is compared to the one from the most central (0-8%) collisions to measure possible modifications and also to that in 7 TeV pp collisions to study the modification of the fragmentation of the correlation strength in Pb-Pb collisions.

Contents

1 Summary

The most successful theory explaining the strong interactions is Quantum Chromodynamics (QCD). The strong force is responsible for the confinement of quarks and gluons into hadrons. At extremely short distances, where the coupling constant is very small, the partons (quarks and gluons) experience a phenomenon namely asymptotic freedom. Asymptotic freedom leads us to conclude that at extremely high temperatures and densities matter is a weakly interacting system of QCD degrees of freedom called Quark Gluon Plasma (QGP). Since the 1970's physicists have been trying to find an experimental way to prove the existance of this phase of matter by creating it and measuring its properties. This state of matter can be created by colliding high energy heavy atomic nuclei at high energies [1].

Ultra-relativistic heavy ion collisions allow investigating the form of matter in extreme temperatures and densities created in laboratory. This possibility helps to understand the dynamics of matter and the physics dominating it on hadronic scales. The medium created in ultra-relativistic heavy ion collisions is a subject to study the QCD. The QCD predicts that partons experience different in-medium energy loss in high energy density matter, so that heavy quarks lose less energy inside the medium compared to lighter quarks. To study this property, we need to utilize a probe inside the medium. Heavy quarks, charm and beauty, are produced on a very short time scale in initial hard scattering processes and consequently undergo the whole collision history. Thus they can be used as probes to characterise the QGP formed in ultra-relativistic heavy ion collisions through their modified yield compared to pp collisions. Heavy flavour hadrons can be studied by measuring electrons from their semi-leptonic decays [2].

ALICE (A Large Ion Collider Experiment) is the dedicated heavy ion detector at the CERN LHC which focuses on hot, dense QCD matter. ALICE is designed to study the physics of strongly interacting matter and the Quark-Gluon Plasma at extremely high energy densities and temperatures in nucleus-nucleus collisions. The design of the ALICE detector is such that the particles produced in the collisions are measured in the most complete way possible, so that the evolution of the system in space and time can be reconstructed and studied. To achieve this goal, many subdetectors are used within ALICE detector that each provides a different piece of information [3].

One way to study the QGP properties, e.g. modification of parton fragmentation function and energy loss is to study the heavy flavour electrons (trigger particles) by correlating them with charged hadrons (associated particles) in azimuth. The correlation on the same side as the trigger particle is called the near-side ($-\pi/2 < \Delta\phi < \pi/2$) and 180° from the trigger particle is called the away side ($\pi/2 < \Delta\phi < 3\pi/2$). The near and away-side yields are used to study the QGP properties. In this analysis, the yields from different centralities in Pb-Pb collisions are compared. They are also compared to the yield from pp collisions at $\sqrt{s_{NN}} = 7$ TeV. The corresponding analysis note can be found in [4].

The analysis is performed on semi-central ($20 - 50\%$) Pb-Pb collisions at center of mass energy $\sqrt{s_{\mathrm{NN}}} = 2.76$ TeV with the ALICE experiment. The azimuthal angular correlation of

heavy flavour decay electrons and charged hadrons is obtained and the near-side yield of the correlation distribution of heavy flavour electrons and charged hadrons is extracted. For the analysis the detectors used are Inner Tracking System (ITS) with $|\eta| < 0.9$, Time Projection Chamber (TPC) with $|\eta| < 0.9$ and Electromagnetic Calorimeter (EMCal) with $|\eta| < 0.9$ and $80° < \phi < 180°$.

2 Introduction

2.1 Asymptotic freedom

Four fundamental forces have been identified in nature: gravitational, electromagnetic, weak and strong force, which in our universe they have different properties. Each force acts through exchanging of a particle. The strength of each force exerted in an interaction is determined by coupling constant which is a dimensionless constant. There is a huge difference between coupling constants of different forces in low energies, from $\alpha_g = 10^{-39}$ for gravitational force to $\alpha_w = 10^{-6}$ for weak force, $\alpha_e = 1/137$ for electromagnetic and $\alpha_s = 1$ for strong force [5]. By increasing the energy, the coupling constant rises for electromagnetic and gravitational force and drops off for the weak and strong forces.

Strong interaction manifests itself through color charged particles, quarks and gluons. It is a very strong force but finite and short-ranged, as it acts only over ranges of nucleus size and responsible to hold the nuclei inside atoms. At very short distances inside the nucleons (or equivalently at high Q^2 in the energy scale) this force gets weaker so that the quarks freely move inside the hadrons. This phenomenon is called asymptotic freedom, because quarks and gluons reach to a state that they can freely move freely within hadrons. In Quantum Chromodynamics the coupling constant diminishes with the expression below:

$$\alpha_s(Q^2) = \frac{12\pi}{(33 - 2n_f)ln(\frac{Q^2}{\Lambda^2_{QCD}})}, \tag{1}$$

where n_f is the number of flavours, Q^2 the momentum transfer and Λ_{QCD} is the QCD scale. At extremely high temperatures and energy densities, quarks and gluons are asymptotically free. This state of matter is called "Quark Gluon Plasma" (QGP). This new state of matter is color neutral medium consisting of freely moving quarks and gluons [5].

2.2 Quark Gluon Plasma

The early development of the universe is well-described by the most prevailing cosmological model, namely the big bang theory. The early universe after the big bang was extremely hot and dense that particles were ultra-relativistic. The energy density was so high that strongly interacting partons "quarks and gluons" interacted weakly. According to Quantum Chromodynamics, this is explainable with asymptotic freedom. This phenomenon leads to an interesting result. At extremely high temperatures and energy densities, QCD degrees of freedom (quarks and gluons) become free such that they deconfine from hadrons and transform into a new system, namely "Quark Gluon Plasma" (see figure 1). At the very beginning ∼10 picoseconds after the big bang this phase of matter which was in sort of a fireball was created which lasted for some 10 microseconds until it expanded and cooled until it transformed to confined state of matter, the hadronic phase.

The phase transition from the quark gluon plasma to baryonic matter is an important subject of study for both theoretical and experimental physicists. There are some experiments ongoing associated with the phase transition that involve the collisions of relativistic heavy ions which can lead to the creation of QGP. In these experiments, massive particle detectors are used to yield information about the phase transition from baryonic matter to QGP (see figure 2) [8].

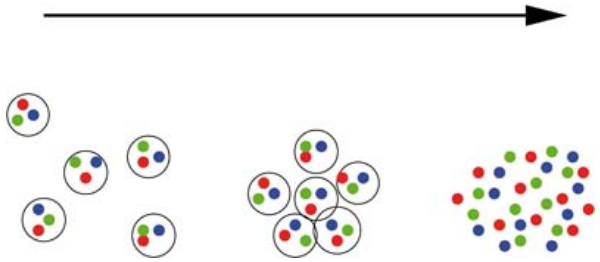

Figure 1: The transition from a hadron gas to a quark gluon plasma. The arrow indicates growing temperature and chemical potential for baryons.

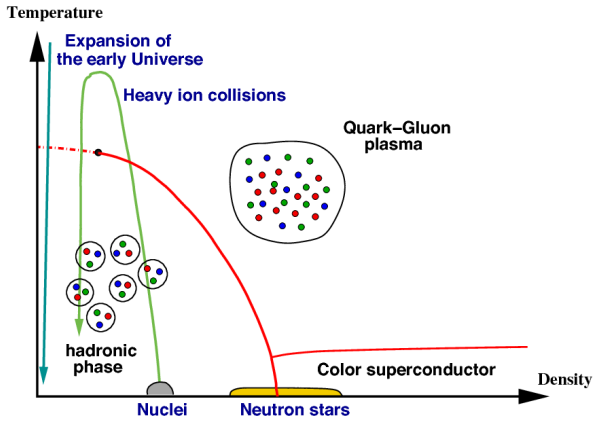

Figure 2: Sketch of the QCD phase diagram as a function of temperature and density. The solid red line denotes the first-order phase transitions, whereas the dashed red line a rapid crossover.

2.3 Phase transition

To transit from hadronic state to Quark Gluon Plasma there must be a thermodynamical equilibrium of the two phases. This phase transition happens in a certain critical temperature. Due to several estimates, the critical temperature that confined matter transits into deconfined matter is of the order of 100 MeV. Separate experiments and analyses have obtained different numbers for critical temperature. Initially, researchers at the CERN-SPS and at RHIC obtained a temperature of 170 MeV with a systematic error of about 10% for a system involving the two light quarks (u and d) and one heavier quark (s) [6]. Later, a

slightly lower critical temperature of $150 - 160$ MeV was obtained at the CERN-LHC [7].

The zero temperature ground state of QCD is significantly different from the high temperature QGP where color charges are confined to the interior of individual hadrons and chiral symmetry is broken spontaneously. Consequently, as the plasma cools some rapid changes in thermodynamic observables occur from the high temperature QGP phase to the low temperature confining and chiral symmetry breaking phase, where the quarks and gluons combine to form colorless states of hadronic matter.
It is possible to estimate the transition temperature by comparing the QGP gas pressure with that of hadronic gas. The lightest hadrons are pions and for $T < 1$ GeV we might expect a gas of relativistic pions. This is a system with 3 degrees of freedom, g=3, so the energy density and pressure of the system are:

$$\rho_\pi = \frac{3\pi^2}{30}T^4, P_\pi = \frac{3\pi^2}{90}T^4. \tag{2}$$

Pions are collective excitations of non-perturbative QCD vacuum. According to the non-perturbative QCD, total pressure of hadronic phase is:

$$P_{low} = B + \frac{3\pi^2}{90}T^4. \tag{3}$$

where B is the bag constant equal to 200 MeV and determined by fits to the masses of physical hadrons [8]. On the other hand, the pressure of the QGP phase with $n_f = 2$ is $P_{QGP}=\frac{37\pi^2}{90}T^4$. Equating two pressures, we find the transition temperature,

$$T_c = (\frac{45B}{17\pi^2})^{1/4} \sim 180MeV, \tag{4}$$

The QGP can be created by heating matter up to a temperature of 2 trillion K which amounts to 170 MeV. This can be accomplished by colliding two heavy nuclei at high energies.

2.4 Relativistic heavy ion collisions

To perceive the dynamics of Quark Gluon Plasma and consequently the early universe, we need to create it in lab-scale. During 1980s and 1990s particle physicists studied the QGP at CERN-SPS accelerator. In 2000 the particle physicists announced that they have found an indirect evidence for a new state of matter [9]. The RHIC accelerator also started its operation in the same year. At present, the LHC collider is continuing this effort by colliding ultra-relativistic lead (Pb) ions.

At the Large Hadron Collider, two beams of lead ions are accelerated to ultra-relativistic velocities and collided with one another. Due to the ultra relativistic velocities, nuclei are Lorentz contracted as illustrated in figure 3. Immediately after the collision, a fireball is produced which undergoes the whole evolution process before decaying into numerous particles, later detected by detectors. At early stages after the collision, particle production is dominated by initial hard scatterings which can be described by perturbative QCD. This stage is often called pre-equilibrium stage [10].

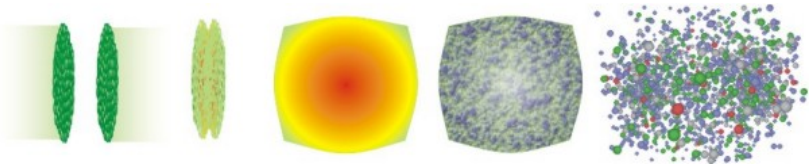

Figure 3: A schematic view of an ultra-relativistic heavy ion collision. From left to right: nuclei before collision are Lorentz contracted, collide, QGP is created, QGP cools and expands, hadronizes and finally freezes out [11].

During next stage, hydrodynamical expansion, many more soft particles emerge from collisions where less momentum is exchanged. These produced particles spread through the medium, and the medium thermalizes in a thermalization time of $\tau_0 \sim 1$ fm/c. After this stage, the medium can be described by hydrodynamics. So that the microscopic properties of the fluid can be replaced by macroscopic observables such as energy density and temperature. If the energy density of the initial collision is large enough and thermalizes in a short time, QGP can be created. When the QGP is generated, it can go through a phase transition and subsequently undergo the next stage, thermalization [10].

During this stage, the fireball expands and cools until the thermal equilibrium becomes unstable since the temperature and the energy density are no longer sufficient. At an estremely short time $\tau \sim 15$ fm/c, the QGP particles freeze out and traverse the medium without further strong interactions and stream towards the detectors. During the freeze-out various particles are produced that before reaching the detectors they will undergo the final state by interacting through Coulomb force and decay to lighter stable particles [10].

2.5 Signatures of the Quark Gluon Plasma

Heavy ion experiments are challenging since the created fireballs are very short-lived and handling hundreds of particles in the detector is difficult. To probe the QGP, we need to observe as many particles as possible and then to retrace the initial formation of the QGP by using the observed data. There are several signatures that prove the presence of the QGP. Some of these signatures are discussed below:

J/ψ suppression

J/ψ suppression is a strong signature for presence of the QGP. Due to gluon fusion, charm and anti-charm quarks are formed within the QGP medium. But due to color screening, charm and anti-charm quarks pair up less as quarkonium states and instead they tend to pair up with lighter quarks. Debye screening of quark color charge is the basic mechanism of deconfinement in QGP. In this mechanism, the screening radius becomes more than the binding radius of the quark system, e.g. radius of the hadron, which means the confining force no longer will be able to keep the quarks together and deconfinement steps in. Due to this, the total number of produced J/ψ mesons and other quarkonium states reduces in heavy

nucleus-nucleus collisions compared to pp and p-Pb collisions [13].

Elliptic flow

The azimuthal momentum distribution of hadronized partons can be utilized to study the properties of the QGP. In heavy ion collisions, ions can collide with different impact parameters [1] which gives a centrality range from 0% for the most central to 100% for the most peripheral collisions. The momentum distribution of the produced partons is in the form of equation 5.

$$E\frac{\mathrm{d}^3N}{\mathrm{d}^3\mathbf{p}} = \frac{1}{2\pi}\frac{\mathrm{d}^2N}{p_\mathrm{T}\mathrm{d}p_\mathrm{T}\mathrm{d}y}(1+\sum_{n=1}^{\infty} v_n\cos[n(\varphi-\Psi_\mathrm{RP})]), \tag{5}$$

where E is the energy of the particle, $\mathbf{p}$ the momentum, p_T the transverse momentum, φ the azimuthal angle, y the rapidity, and Ψ_RP the reaction plane angle [14]. The coefficients v_n characterize the momentum anisotropy. The coefficient v_1 is called directed flow, whereas v_2 is called the elliptic flow. The elliptic flow originates from the interaction between particles produced in asymmetric region of space (the almond-like shape in Figure 4). Elliptic flow (v_2) characterizes the azimuthal asymmetry of the momentum distribution. The first measurements of v_2 at RHIC [15] showed that v_2 is quite large and approaches the prediction of perfect hydrodynamics. The agreement of v_2 with perfect hydrodynamics is interpreted as a signature of the very fast thermalization of the system and is considered as an important discovery at RHIC leading to the concept of strongly interacting QGP [16].

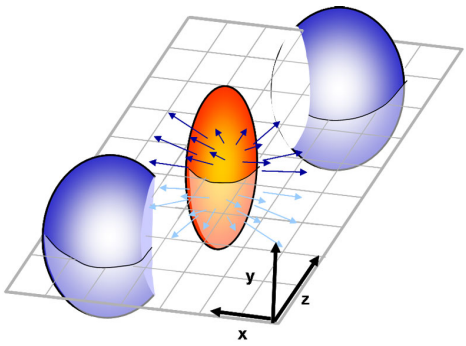

Figure 4: Interaction volume (almond-like shape) after a non-central collision of two nuclei. The spatial anisotropy translates into a momentum anisotropy of the produced particles (anisotropic flow).

Jet quenching

Jet quenching in Pb-Pb collisions is another probe of the QGP. Jets consist of high p_T particles and they are a result of initial hard scatterings of the incoming partons. They are

[1] Impact parameter is the length of the vector connecting centers of the colliding nuclei in the plain transverse to nucleus trajectories.

produced in pairs within a shorter time scale compared to the QGP formation time. Thus jets can traverse the hot and dense medium (QGP). These jets lose energy through gluon radiation due to high color density of the medium. Due to energy loss of the partons, the jet in the opposite direction which traverses less inside the medium, loses less energy.

There are enough evidences to prove jet quenching in heavy ion collisions. The azimuthal angular correlation of high p_T particles for pp, d-Au and Au-Au from STAR experiment is shown in figure 5. It can clearly be seen from the correlation at $\Delta\phi = \pi$ that for Au-Au collisions there is no peak on the away-side [17].

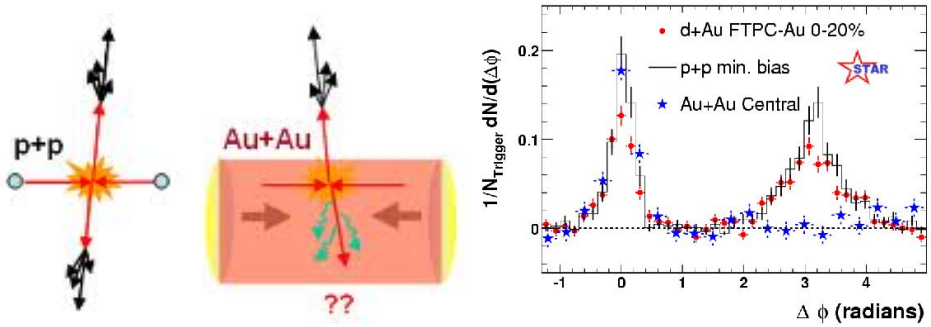

Figure 5: Hard pp collisions resulting in two jets (left panel). Au-Au collisions where the jet far from the vacuum loses energy in the medium and does not make the way out (central panel) [18]. Comparison of two-particle azimuthal angular distributions for central d-Au, pp and Au-Au collisions (right panel) [17]

.

2.6 Heavy Flavour Physics; theoretical background

The aim of the ultra-relativistic heavy ion collisions is to create the QGP and study its characteristics under controlled laboratory conditions. Right after the collision, the partons of incoming nuclei go through hard collisions. In the elementary pp collisions these partons will fragment into jets of high transverse momentum which can be measured in the detectors. However in heavy ion collisions these jets will slow down while traversing through the medium created right after the collision. The QGP properties can be studied by measuring the attenuation rate of these jets. This phenomenon (jet quenching) is an evidence for energy loss of partons traversing through this hot, dense medium [19].

The dependence of parton energy loss on color charge and quark mass leads us to use heavy quarks (charm and beauty) as perfect probes. Furthermore, heavy quarks are much heavier than light quarks, like up and down quarks, which means they dominate the QGP matter and they are not affected much by the chiral symmetry breaking [20]. As a result of their high masses, they are produced mainly in the initial phase through gluon fusion processes in the heavy ion collisions (shown in RHIC measurements [21],[22]). Heavy flavour production

can also happen later through thermal processes at low transverse momentum [19].

The particle production yield of heavy ion collisions depends on both initial and final state effects. We can quantify them by using R_{AA}, the nuclear modification factor, which is a ratio of the yield from heavy ion collision to yield from pp collisions scaled by the number of binary collisions. R_{AA} can be used to compare the energy loss of the different particles produced in the QGP. According to the theoretical models based on perturbative QCD, heavy quarks lose less in medium energy than light quarks which is due to the suppression of gluon radiation at small angles (Dead-cone effect) [23-25]. This angle depends on the mass of the particle so we can expect that charm quark loses less energy traversing through the medium compared to light quarks like pion. We can also conclude that beauty quark is suppressed less than charm quark. As a result, the nuclear modification factors should be dependant on the mass of the hadrons, $R_{AA}^{\pi^{\pm}} < R_{AA}^{D} < R_{AA}^{B}$ [19].

2.7 Heavy flavour decay electrons

The electrons can be utilized as probes to study the properties of the QGP. The semi-leptonic decay of D and B mesons gives rise to investigate open charm and beauty production. The electrons produced through semi-leptonic decay of D and B mesons are mixed with electrons coming from other sources known as non heavy flavour electrons (photonic electrons). Therefore, the identification of electrons is necessary by invariant mass method (see chapter 5).
There are two ways to identify heavy flavour electrons. The first method is to subtract the cocktail of background electrons from inclusive electrons. The second method is based on the displacement of beauty decay electrons regarding the primary vertex by the large decay length of B mesons ($\tau \sim 500$ μm). The beauty decay electrons can be extracted by the track impact parameter [26].

3 The ALICE experiment

The Large Hadron Collider (LHC) in Geneva is the largest and the most powerful particle collider since 2009. The highest energy that it reaches now is a center of mass energy $\sqrt{s} = 7$ TeV for pp collisions and it will reach $\sqrt{s_{\mathrm{NN}}} = 5.02$ TeV for Pb-Pb collisions. ALICE, the acronym for A Large Ion Collider Experiment, is one of the detectors at the LHC, is focused on the study of heavy ion collisions. The main focus of ALICE is to study QCD related effects and it is the only dedicated heavy ion experiment at the CERN-LHC. A layout of this detector is shown in figure 6.

ALICE is a large experiment with $16 * 16 * 26\ m^3$ and a weight of ten thousand tons, thus it cannot be a single detector and like other particle detectors it consists of different layers of subdetectors. Each layer has a different task and detects different properties of the particles going through. It can be split into a central barrel situated within L3 solenoid magnet, the muon forward arm, a cosmic detector and some subdetectors very close to the beam pipe [28].

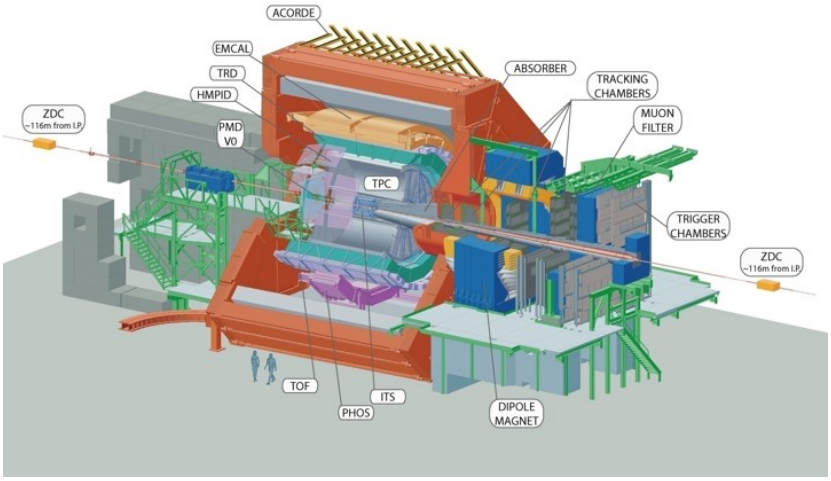

Figure 6: Layout of the ALICE detector.

3.1 ALICE coordinate system

The standard coordinate system of ALICE detector is a right-handed cartesian coordinate system where the origin is located in the interacting point (IP) of the colliding particles. From the origin the z axis is along the beam pipe, the x axis points towards the center of the LHC. ϕ (azimuthal angle) is the angle around the z axis, θ indicates an angle from z axis and r is simply the distance from the origin.
Rapidity is always used in particle physics as a measure of velocity relative to a reference frame defined as $\phi = \arctan(v/c)$. But since it is hard to measure the speed of particles, we can assume that the mass of the particles is almost zero and the velocity nearly equal to

speed of light and define the pseudo-rapidity $\eta = -\ln(\tan(\theta/2))$, which only depends on the polar angle, θ [28].

3.2 Central detectors

The magnet of the ALICE detector is remained from the previous experiment (L3) which was prior to LHC. The magnet is now known as L3 magnet and the detectors inside the magnet are called the central barrel. The central barrel covers $|\eta| < 0.9$ and the whole azimuthal angle. The detectors inside the magnet are used for tracking and identification of electrons and hadrons [28]. From inside out, the central barrel consists of the Inner Tracking System (ITS), Time Projection Chamber (TPC), Transition Radiation Detector (TRD), Time Of Flight (TOF), a Ring Imaging Cherenkov detector called the High Momentum Particle Identification Detector (HMPID), the Photon Spectrometer (PHOS) and Electromagnetic Calorimeter (EMCal). Except for the last three detectors, all these detectors cover the full azimuth. In addition to these detectors, the Photon Multiplicity Detector (PMD), Forward Multiplicity Detector (FMD), T0 and V0 are also close to the beampipe [29].

In this thesis, I will cover the subdetectors related to the electron studies. Three of the ALICE subdetectors were engaged. The ITS was used for vertexing and tracking. The TPC was used for primary tracking and particle identification and EMCal was employed for electron identification.

3.2.1 Inner Tracking System (ITS)

The Inner Tracking System (ITS) is located at the center of the central barrel and surrounds the collision position. The ITS consists of 6 cylindrical semi-conductor based detectors which are located at radial distance of about 4, 7, 15, 24, 39 and 44 cm from the beamline. The innermost detectors are 2 Silicon Pixel Detectors (SPD) and going outward radially from the center, 2 Silicon Drift Detectors (SDD) and the outermost detectors are 2 Silicon Strip Detectors (SSD). SPD covers a pseudorapidity range of $|\eta| < 1.98$ unlike the rest of the subdetectors within central barrel. Primary and secondary vertex information as well as p_{T} spectrum for particles with low p_{T} are provided by the ITS [28,29]. Different layers of the ITS detector can be seen in figure 7 .

The ITS is designed for tracking and vertexing with an impact parameter (b) resolution < 65 μm for transverse momentum > 1 GeV/c which is good enough to find the secondary decay vertices [29]. The choice of the slicon detectors was based on the impact parameter resolution. The innermost detectors were selected to be pixel detectors due to the high particle density. For two middle detectors, silicon drift detectors are sufficient. And for the outer two detectors, silicon micro-strips were employed due to the low particle densities.

All ITS detectors except the inner most detectors (SPD) are capable of particle identification by measuring dE/dx for non-relativistic particles, which allows the ITS to be utilized as a low momentum particle spectrometer. The ITS is also used for tracking those low momentum

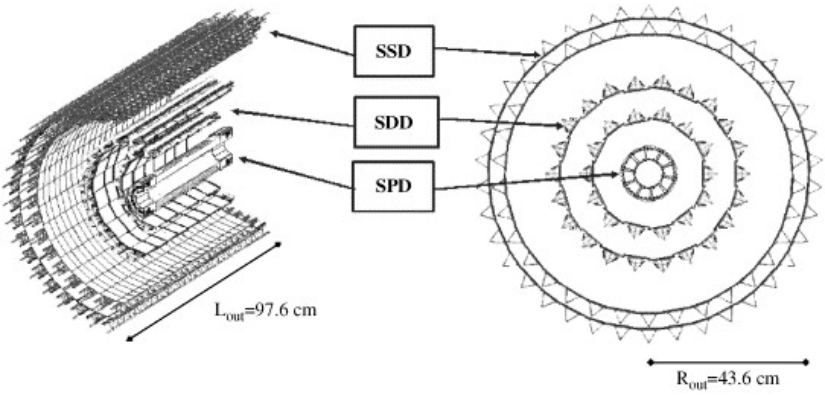

Figure 7: Sketch of the ITS with 6 layers of silicon detectors (SPD, SDD and SSD) used for particle tracking and vertexing.

charged particles ($70 < p_{\mathrm{T}}^{\mathrm{e}} < 200$ MeV/c) which have a too-curved tracks and thus too short of a track for the TPC to be able to reconstruct the track.

3.2.2 Time Projection Chamber (TPC)

The Time Projection Chamber (TPC) is a gas detector within the central barrel. In the heavy ion collisions a very high number of daughter particles are produced, which ALICE is expected to handle. For this reason TPC is built relatively large to generate most of the tracking information, though being slow. Most of the data at ALICE is generated by TPC. It is mainly used for charged particle tracking but it is also used for particle identification by measuring specific ionization energy loss dE/dx and momentum information.

The TPC is a cylindrical detector (see figure 8) around the beam pipe along the z axis. It covers 2π in azimuth and $|\eta| < 0.9$ in pseudo-rapidity with an inner radius of 85 cm, outer radius of 247 cm and 5 m length along the beampipe. The TPC is filled with Ne (85.7%), CO_2 (9.5%) and N_2 (4.8%) gas mixture. The particles going through ionize the gas mixture in it. The electrons from the ionization drift to detectors in each end of the cylinder as a result of the very high voltage in the z direction. This data creates the tracks which with their curvature the momentum and charge of the particle can be measured. Also with the number of ionized electrons dE/dx can be measured. These tracks are matched with the position data from ITS and outer detectors to reach the maximum precision [28],[29].

3.2.3 Electromagnetic Calorimeter (EMCal)

The EMCal is an electromagnetic calorimeter with a limited acceptance (110 degrees azimuthal, from -0.7 to 0.7 in pseudorapidity and $4.35 < R_{EMCal} < 4.7$ m radial distance). It focuses on photon measurements jets by improving jet energy resolution. Additionally, the EMCal is employed for triggering and reconstructing high energy jets in ALICE. It is also

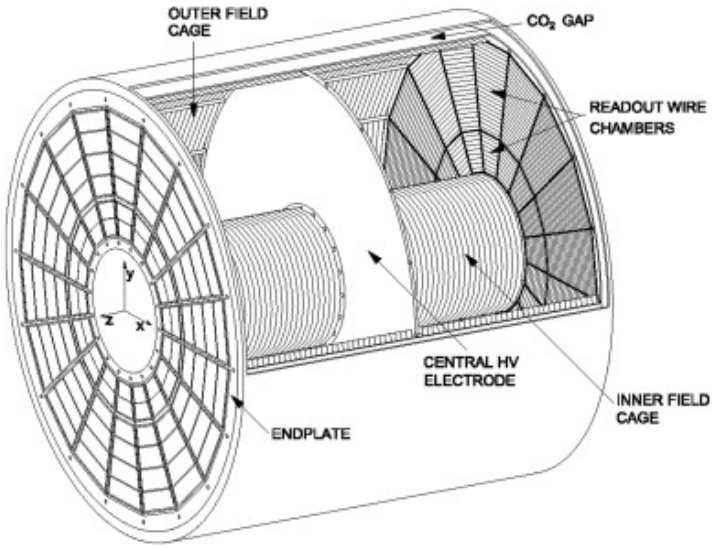

Figure 8: Sketch of the TPC. The active volume (filled with a gas mixure) is divided into two parts by a cathode in the middle. Readout hardware are installed on cathode and anodes.

utilized to measure high momentum photons and electrons and neutral hadrons [33]. The EMCal has a high momentum resolution (0.1 GeV/c to 100 GeV/c for charged particles) which is ideal for measuring the full range of hard and soft jets [28].

The fundamental unit of EMCal design is a module of 4 towers of Pb-scintillators. 12 modules are later grouped into a strip module and 24 strip modules into super modules of 288 modules in total which is 1152 towers (see figure 9) [33]. The scintillators turn the energy deposit of hadrons/photons into more photons, which the optical fibers pick them up and readout on the outside of the detector with an avalanche photodiode sensor [28].

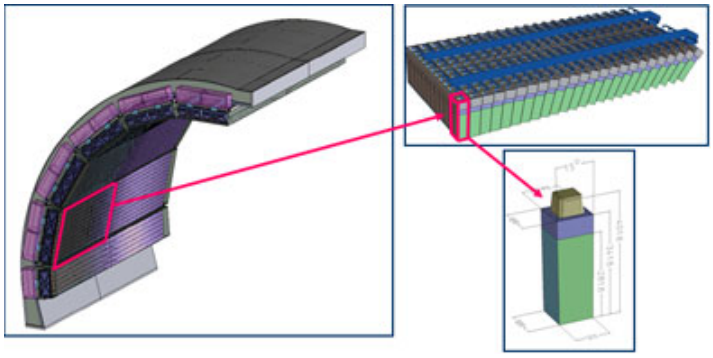

Figure 9: Sketch of the EMCal (left panel), a super module (top-right) and a module (bottom-right).

4 Analysis framework and event selection

The offline framework for the analysis is based on the ROOT software. This software is fully written in C++ programming language and uses C++'s object oriented environment. It offers different ways of interacting with the software, via command line, batch scripts and other graphical interfaces. The main ALICE offline framework is AliRoot, which is designed for data handling and analysis both on real data and Monte-Carlo simulations. In second case, AliRoot is capable of analysing the Monte-Carlo data of the particle interactions at the interaction point, hardware and the signal generated by the detector using GEANT [29].

The ALICE analysis framework has different layers which each layer is associated with a different phase of the analysis. The first layer is related to particle collisions. In this layer, PYTHIA and HIJING, the Monte-Carlo event generators, produce the final state particles with their associated momentum and rapidity. In the second layer, the interactions of these particles with the detector hardware is simulated via GEANT3 transport code. In this layer all events that a particle can go through is taken into account, including particle decay, ionization, scattering, energy deposition, etc [29].

The final information of all reconstructed particles is stored in a file format called Event Summary Data (ESD). But the huge size of the stored information makes it slow and difficult to use. As a result, the information is distilled to files called Analysis Object Data (AOD). The advantage of AOD is that the information is filtered with respect to the users' interest on specific physical phenomena. So if the information is unnecessary, it is not included in the AOD's. The other possibility is that the information can be translated into other forms and restored in AOD [29].

Even by using AODs, the amount of information to be processed is massive and a normal computer cannot handle it. So the data can be distributed over several computers using the GRID which is a cluster of available remote storage elements. Regardless of number of involved computing elements, the computing time for a data analysis with GRID, can range from a few minutes for pp collisions to some days for Pb-Pb collisions [29].

4.1 General strategy

The analysis starts by identifying inclusive electrons using the ALICE detectors. The inclusive electrons contain hadron contamination which are removed by using the scaled hadron-hadron $\Delta\phi$ distribution and subtracting from the electron-hadron $\Delta\phi$ distribution. To construct the heavy flavour decay electrons from inclusive electrons, the non-heavy flavour decay electrons are reconstructed by using invariant mass method. The next step is to construct the azimuthal angular correlation between heavy flavour decay electrons (HFE) and charged hadrons. In this step, the non-heavy flavour decay electrons construction efficiency is calculated and removed from inclusive electron spectrum.

In the next step, we remove the detector effects by using the mixed event correction. Then the final correlation distribution is fit on the near-side with a function which is a sum of a constant, a gaussian and the flow function[2] to extract the yield and in the end the near-side yield from correlation distribution in semi-central Pb-Pb collisions is compared with the one from Pb-Pb collisions and 7 TeV pp collisions.

4.2 Dataset and event selection

This analysis is performed on the 2011 Pb-Pb collisions (LHC11h) dataset collected by the ALICE detector. This analysis is done for 20−50% centrality selection. Centrality distribution in Pb-Pb collisions with semi-central trigger is shown in figure 10. The $20 - 50\%$ centrality events are selected from the dataset acquired using a logical OR of minimum bias and semi-central trigger. The centrality is estimated using multiplicity in the VZERO detector.

The analysis output is obtained with the lego train using aliroot version v5-04-48-AN for semi-central analysis. The run number used for the analysis are selected from run condition table labelled as good runs and some quality checks performed for PID measurements. The run list is as below.

170593, 170572, 170388, 170387, 170315, 170313, 170312, 170311, 170309, 170308, 170306, 170270, 170269, 170268, 170230, 170228, 170207, 170204, 170203, 170193, 170163, 170159, 170155, 170091, 170089, 170088, 170085, 170084, 170083, 170081, 170040, 170027, 169859, 169858, 169855, 169846, 169838, 169837, 169835, 169591, 169590, 169588, 169587, 169586, 169557, 169555, 169554, 169553, 169550, 169515, 169512, 169506, 169504, 169498, 169475, 169420, 169419, 169418, 169417, 169415, 169411, 169238, 169167, 169160, 169156, 169148, 169145, 169144, 169138, 169099, 169094, 169091, 169045, 169044, 169040, 169035, 168992, 168988, 168826, 168777, 168514, 168512, 168511, 168467, 168464, 168460, 168458, 168362, 168361, 168342, 168341, 168325, 168322, 168311, 168310, 167988, 167987

The analysis is performed on AOD sample (AOD 115) which is selected using the physics selection and requiring primary vertex from tracks with a z co-ordinate in the range $|z| < 10$ cm. The number of events analysed is 13M for the semi-central dataset.

4.3 Monte-Carlo samples

To calculate the Non-HFE reconstruction efficiency (details in next section), the Monte-Carlo sample with enhanced π^0 and η is used.

Dataset: `LHC12a17e_fix` for $20 - 50\%$ central events.

Event generator : Hijing 2012, electrons, LHC11h anchor runs.

[2] $2v_2^{trig}v_2^{asso}\cos(2\Delta\phi)$

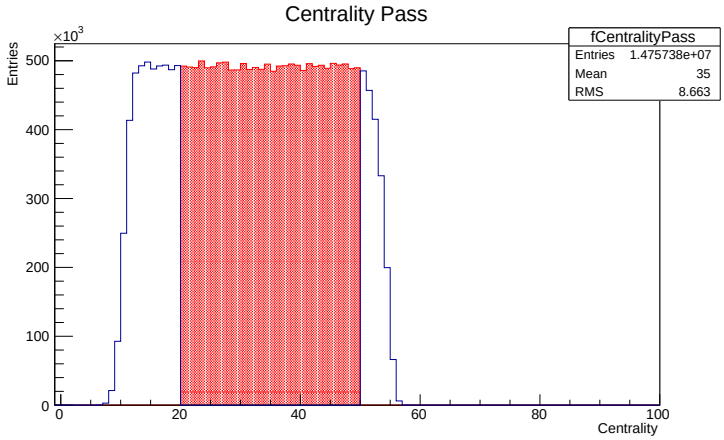

Figure 10: Centrality distribution in Pb-Pb collisions with semi-central trigger.

5 Heavy flavour electron identification

In this chapter the electron identification methods and the applied selection cuts are discussed.

5.1 Track reconstruction and selection

Tracks are selected for electron identification by applying several track selection cuts. AOD tracks which pass filter mask `AliAODTrack::kTrkGlobalNoDCA` are considered for electron identification. Other additinal cuts are applied which are summarized in table 1.

Table 1: Track selection cuts for electron identification

Track property	Cut applied
Min number of TPC clusters	100
Min number of ITS cluster	3
Min ratio of TPC clusters	0.6
Max χ^2 per TPC cluster	3.5
Max χ^2 per ITS cluster	-1
η range	(-0.7, 0.7)
Reject kink candidates	yes
Hit in any SPD layer	yes
ITS and TPC refit	yes

The charged particle tracks reconstructed using the ITS and TPC are propagated towards the EMCal detector using the Kalman filter approach. The tracks which have geometrical matching with EMCal cluster are selected as electrons.

5.2 Electron identification

In this analysis, the electron identification is performed using information from the TPC and EMCal. For the TPC we use the number of Nσ defined as the measured dE/dx signal in the detector minus the expected value for electrons divided by the resolution. To extend the p_{T} reach of electrons and to separate electrons from hadrons in a wider momentum range we use the EMCal detector. For each track, the momentum information is provided with the track reconstruction algorithm in the TPC and ITS. The corresponding energy deposit E is measured in the EMCal. Particle tracks with E/p ratio around 1 are identified as electrons since the mass can be neglected for relativistic electrons.

In addition to E/p ratio, we also use the parameters describing the shape of the shower created by particles in the EMCal detector to improve the purity of electron sample. Shower shapes are obtained from the elliptical parametrization of clusters in the EMCal detector. The parameters give the energy spread along both ellipse axes, and are named as M02 for the long axis and M20 for the short.

The optimum values for $\sigma_{\mathrm{TPC-d}E/\mathrm{d}x}$, E/p and shower shape cuts were selected by calculating the purity of electron identification. Figure 11 shows the $\sigma_{\mathrm{TPC-d}E/\mathrm{d}x}$ (with respect to the

dE/dx expected for electrons) as a function of momentum and the shower shape parameters (long axis and short axis) versus E/p distribution for the semi-central dataset.

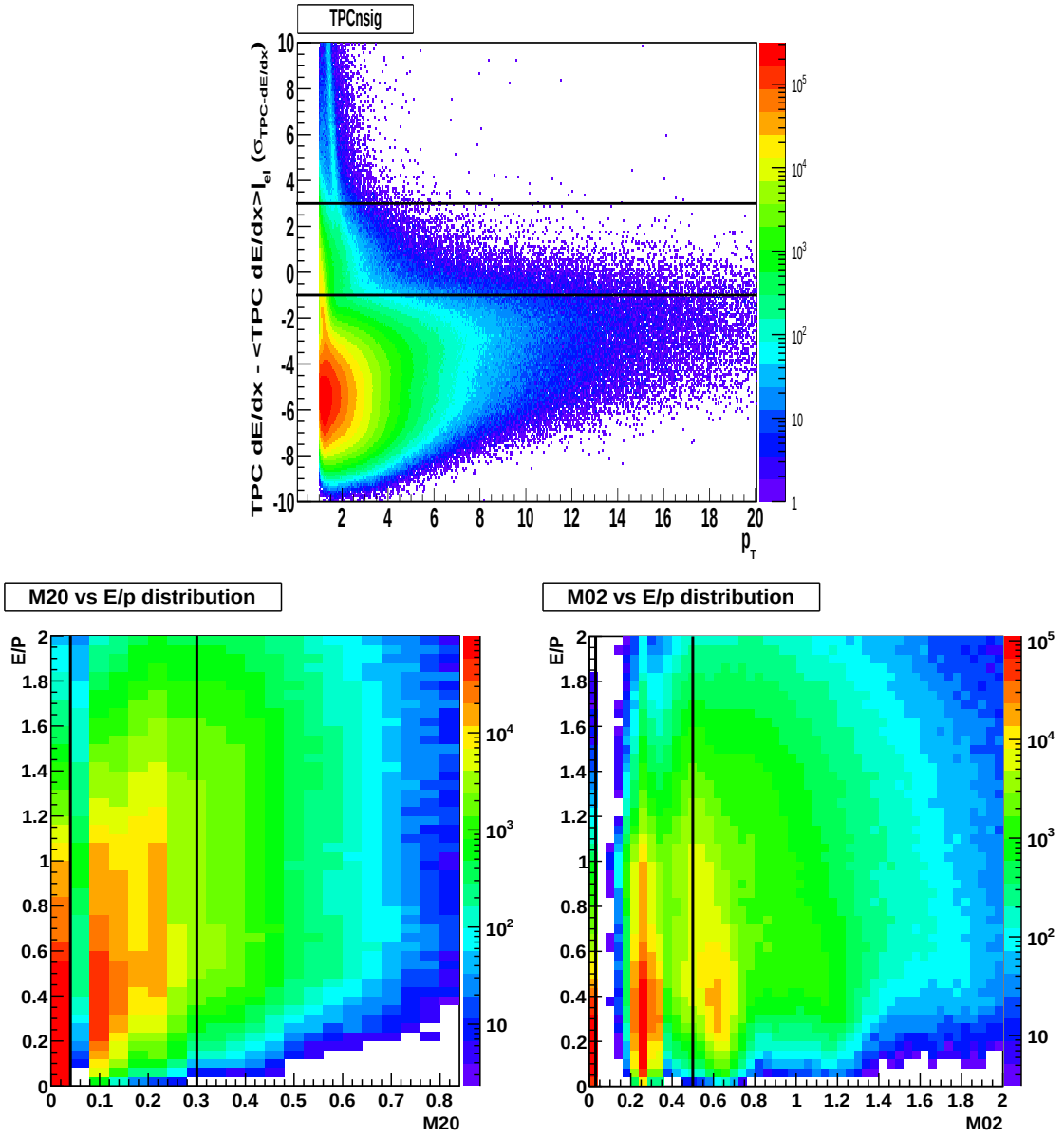

Figure 11: $\sigma_{\mathrm{TPC-d}E/\mathrm{d}x}$ (top panel) and shower shape versus E/p distribution (bottom panel) for semi-central Pb-Pb collisions.

The optimum value for $\sigma_{\mathrm{TPC-d}E/\mathrm{d}x}$ is selected by looking at the E/p distribution for different values of $\sigma_{\mathrm{TPC-d}E/\mathrm{d}x}$ values. Figure 12 shows the E/p distribution for different values of $\sigma_{\mathrm{TPC-d}E/\mathrm{d}x}$ for semi-central dataset.

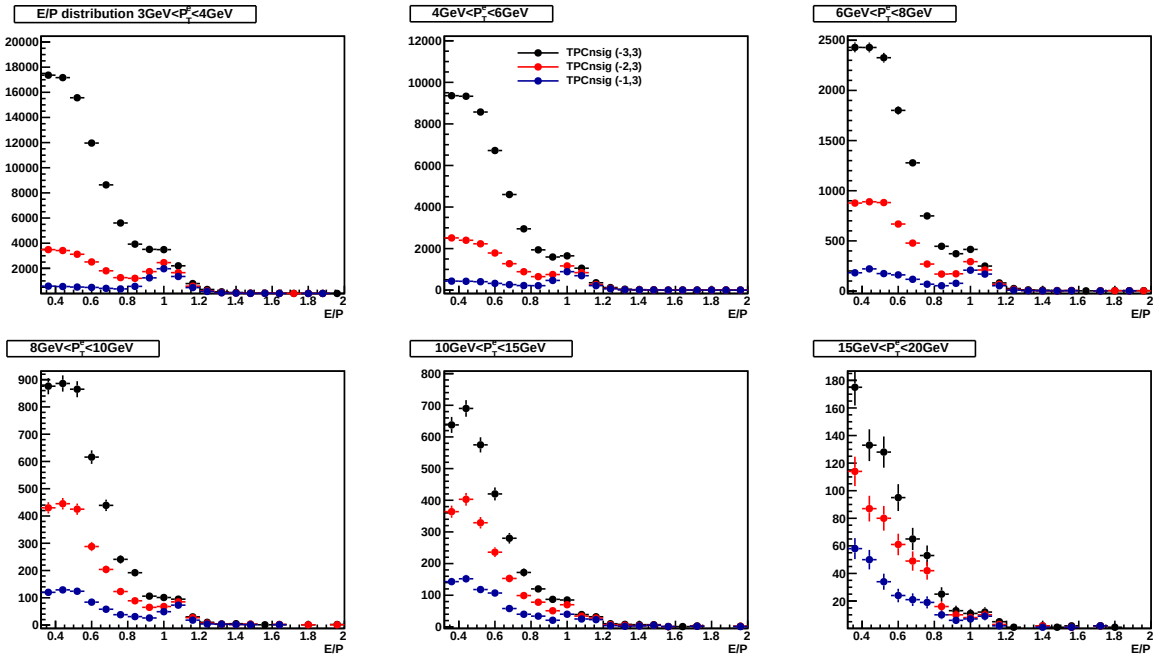

Figure 12: E/p distribution for different $\sigma_{\mathrm{TPC-d}E/\mathrm{d}x}$ for $3 < p_{\mathrm{T}}^{\mathrm{e}} < 20$ GeV/c in semi-central Pb-Pb collisions.

Since 3σ leaves a lot of hadron contamination in the sample and 1σ removes more signal, the optimum values for $\sigma_{\mathrm{TPC-d}E/\mathrm{d}x}$ selected was $-1 < \sigma_{\mathrm{TPC-d}E/\mathrm{d}x} < 3$ for semi-central collisions. Fixing these $\sigma_{\mathrm{TPC-d}E/\mathrm{d}x}$ values, the E/p distribution for different shower shape cuts are determined and shown in figure 13.

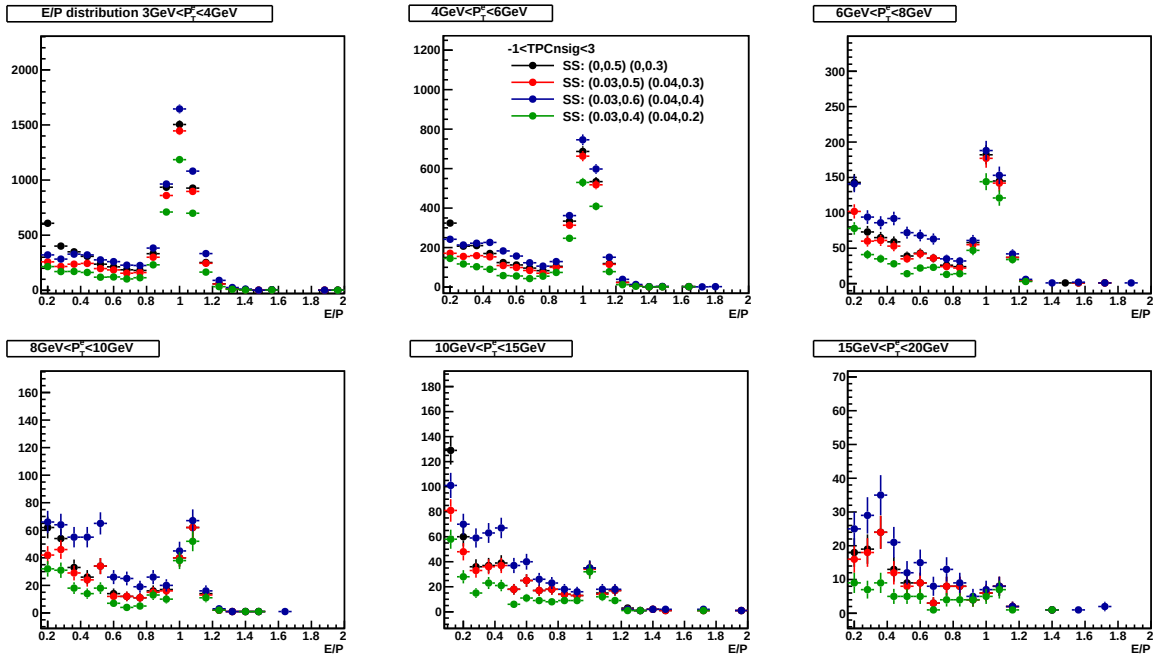

Figure 13: E/p distribution by applying different shower shape cuts for $3 < p_{\mathrm{T}}^{\mathrm{e}} < 20$ GeV/c in semi-central Pb-Pb collisions.

The hadron contamination can be obtained by taking E/p ratio for hadrons ($-5 < \sigma_{\mathrm{TPC-d}E/\mathrm{d}x} < -3.5$) after applying shower shape cuts scaled to match the E/p distribution for $E/p < 0.4$ as shown in figure 14. The purity, corresponding to each shower shape cut value for E/p between 0.8 and 1.2, is shown in figure 15 for the semi-central dataset. The purity is calculated as the ratio of number of all electron candidates minus number of hadrons to number of all electron candidates for $0.8 < E/p < 1.2$

$$Purity = \frac{N^{AllE} - N^{Had}}{N^{AllE}}. \tag{6}$$

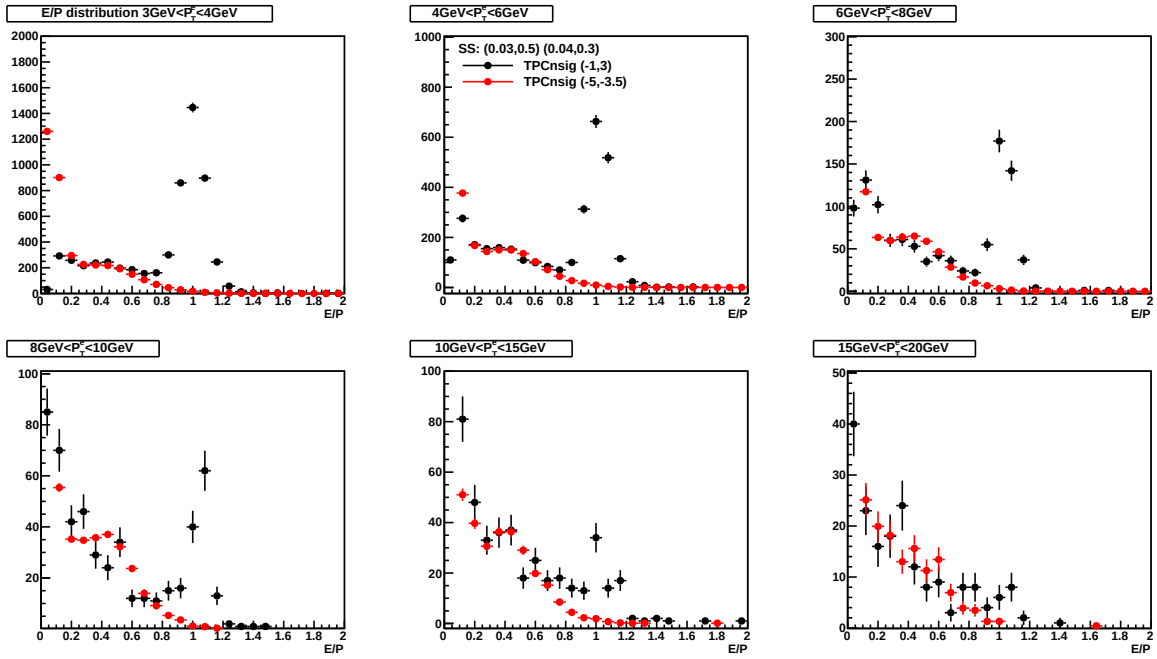

Figure 14: E/p distribution for $0.03 < M02 < 0.5$ and $0.04 < M20 < 0.3$ with hadron contamination estimation for semi-central Pb-Pb collisions.

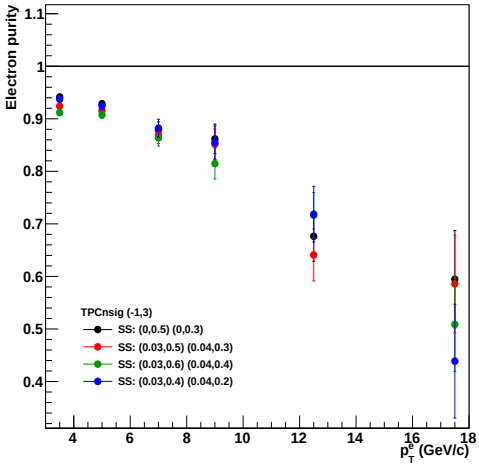

Figure 15: Electron purity for different shower shape cuts for semi-central Pb-Pb collisions.

Since the purity and efficiency should be optimally considered for electron identification such that considerable amount of hadron contamination is removed while preserving most of the signal, the shower shape cut value selected is set 2. Figure 15 shows that the electron purity for set 2 drops from 92% at low p_{T} ($p_{\mathrm{T}} = 3.5$ GeV/c) to 60% at high p_{T} ($p_{\mathrm{T}} = 17.5$ GeV/c). The values for $\sigma_{\mathrm{TPC-d}E/\mathrm{d}x}$, E/p and shower shape parameters are summarized in table 2.

Table 2: Electron identification cuts

Cut parameters	Semi-central
$\sigma_{\mathrm{TPC-d}E/\mathrm{d}x}$	(-1, 3)
Shower shape long axis (M02)	(0.03, 0.5)
Shower shape short axis (M20)	(0.04, 0.3)
E/p	(0.8, 1.2)

The remaining hadron contamination after applying the electron identification cuts are removed using hadrons scaled to E/p distribution.

5.3 Non-heavy flavour electron reconstruction

The inclusive electron spectrum shown in figure 16 consists of several sources:

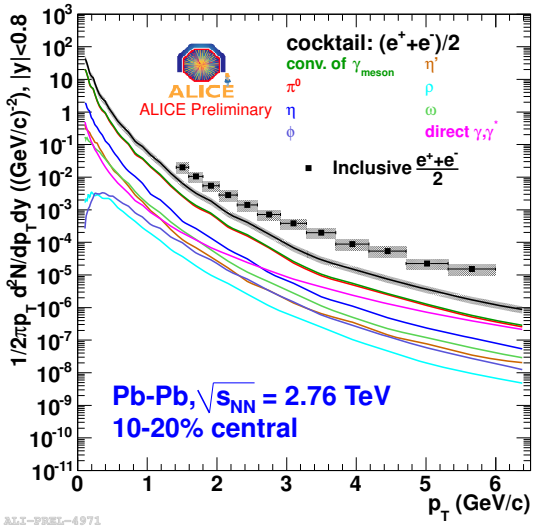

Figure 16: Invariant differential inclusive electron yield in Pb-Pb collisions $\sqrt{s_{\mathrm{NN}}} = 2.76$ TeV, compared to the cocktail of different electron sources

- Heavy flavour electrons from semi-leptonic decay of heavy flavour hadrons,
- Background electrons from Dalitz decays of light neutral mesons and from photon conversion in the detector material,
- Background electrons from weak K $\rightarrow$ e$\pi\mu$ (K_{e3}) decays and dielectron decays of light vector mesons,
- Background electrons from dielectron decays of heavy quarkonia,

- Background electrons originating from partonic hard scattering processes (Drell-Yan processes and prompt photon production).

Of the background contributions listed above, the electrons from Dalitz decay and photon conversions dominate. Contributions from other sources are found to be negligible. Here we reconstruct the dominant sources of non-HFE background.

The invariant mass of e^- , e^+ pairs from conversions and Dalitz decay (which will be refered to as non-HFE sources from here on) is very small while no such correlation exists for HFE. Thus the non-HFE background can be reconstructed by pairing the $e^\pm$ with their partners and calculating their invariant mass.

In this procedure we first apply electron identification criteria to tag one of the $e^\pm$ tracks from primary collision vertex. As a second step we loop over all other tracks in the same event and find the partner electron. AOD tracks which pass filter mask `AliAODTrack::kTrkTPCOnly` are considered for partner electrons. Additional cuts mentioned in table 3 are also applied.

Table 3: Track selection cuts for the associated electron.

Track property	Cut applied
Min number of TPC clusters	80
Min p_{T} (GeV/c)	0.3
TPC and ITS refit	yes
Pseudorapidity	$-0.9 < \eta < 0.9$
TPC cut	$-3 < \sigma_{\mathrm{TPC-d}E/\mathrm{d}x} < -3$

Loose $\mathrm{d}E/\mathrm{d}x$ cut is applied around the electron band for the partner electron to increase the efficiency of finding the electron pair. The invariant mass for these electron pairs are computed from AliKFParticle class. Additionally, NDF > 1 and $\chi^2 < 3$ cuts are applied on the reconstructed mother particle. The invariant mass distribution for like and unlike-sign electron pairs is shown in figure 17.

To reject the photonic electron background, a cut of invariant mass $m < 0.1$ GeV/c^2 is applied for semi-central analysis. The unlike-sign electron pairs contain true non-HFE as well as the combinatorial background, where heavy flavour electrons are accidentally reconstructed as non heavy flavour. The combinatorial background is estimated from the like-sign pairs. The non-HFE can be obtained by removing like-sign paired electrons from the unlike-sign sample:

$$N_e^{NHF-reco} = N_e^{ULS} - N_e^{LS}. \tag{7}$$

5.4 Non-heavy flavour electron reconstruction efficiency

The Non-HFE that are not reconstructed by the invariant mass method are estimated using Non-HFE reconstruction efficiency.

$$N_e^{NHF-notreco} = \left(\frac{1}{\epsilon^{NHFE}} - 1\right) N_e^{NHF-reco}. \tag{8}$$

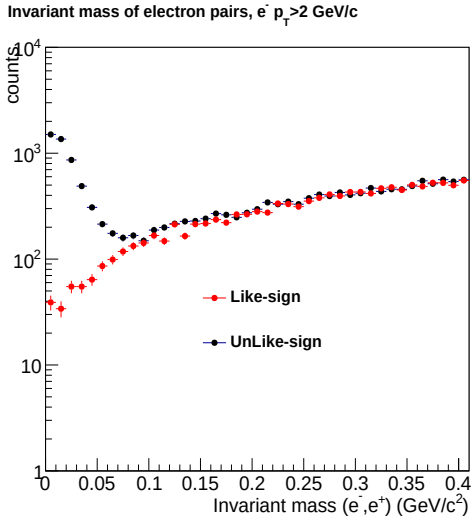

Figure 17: Invariant mass distribution for like (red symbols) and unlike-sign (black symbols) electron pairs for the semi-central Pb-Pb events.

The reconstruction efficiency of Non-HFE using invariant mass method is calculated using the MC sample `LHC12a17e_fix` for semi-central events. It is calculated by applying the same cuts used in the real data analysis. The p_{T} distribution of electrons is biased because of the π^0 and η enhancement in the MC sample [2]. This bias is removed by calculating the weight of π^0 and η enhancement (HIJING/Enhancement) and applying this weight to the p_{T} distribution of electrons.

5.4.1 Weight calculation

The weight is calculated by selecting π^0 and η from HIJING and enhanced π^0 and η events. The ratio of HIJING and embedded p_{T} distribution is calculated. The ratio is fit with a Hagedron function ($\frac{A}{(exp(-B*x-C*x^2)+(x/D))^E}$) as shown in figure 18.

The fit function gives the weight to be applied for electron p_{T} to remove the bias from enhancement. The electron p_{T} is weighed with the value obtained from the fit function with p_{T} of the parent (π^0 and η) as input. The p_{T} distribution of electrons before and after applying the weight is shown in figure 19.

Figure 20 shows the non-HFE reconstruction efficiency as a function of $p_{\mathrm{T}}^{\mathrm{e}}$ before and after applying the weight. The efficiency ranges from 40% at low momentum to 60% above 4 GeV/c.

The heavy flavour decay electron yield can thus be expressed as:

$$N_e^{HF} = N_e^{Incl} - N_e^{NHF-reco} - N_e^{NHF-notreco}. \tag{9}$$

Heavy flavour decay electrons are selected in 4 p_{T} bins from 4.5 to 20 GeV/c. The number of electrons in each $p_{\mathrm{T}}^{\mathrm{e}}$ bin is shown in figure 21 for semi-central Pb-Pb events.

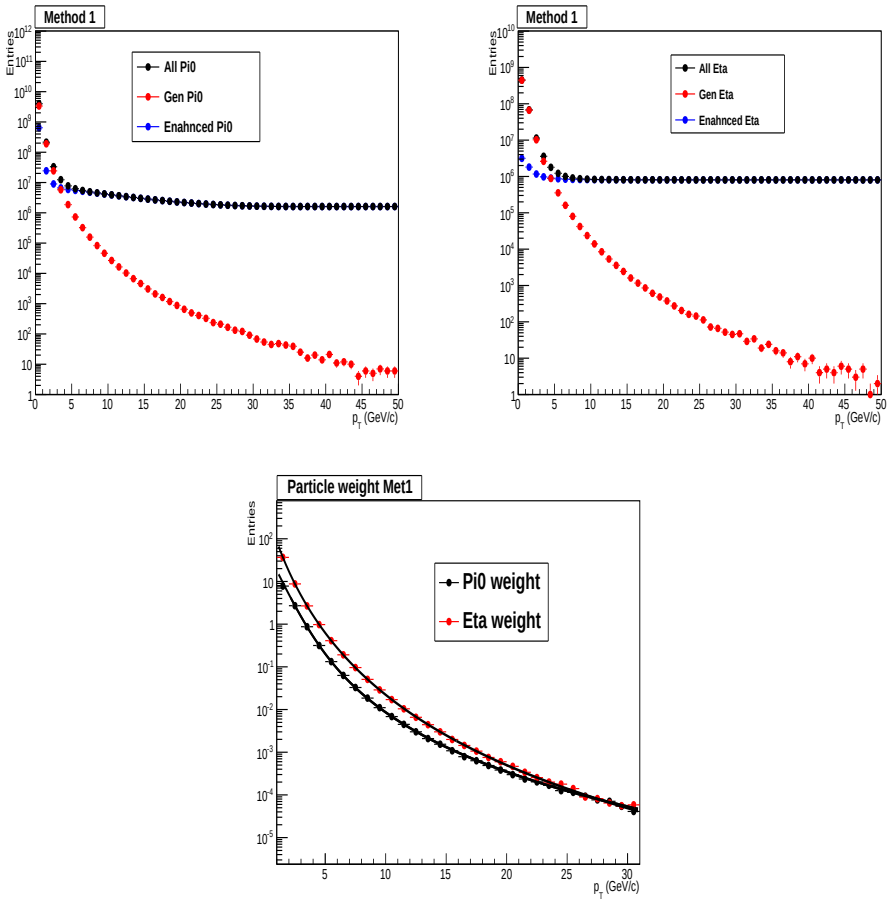

Figure 18: p_{T} distribution of π^0 (top left panel) and η (top right panel) from HIJING and embedded events. Weight = HIJING/Embedded p_{T} distribution fit with a hagedron function for π^0 and η (bottom panel).

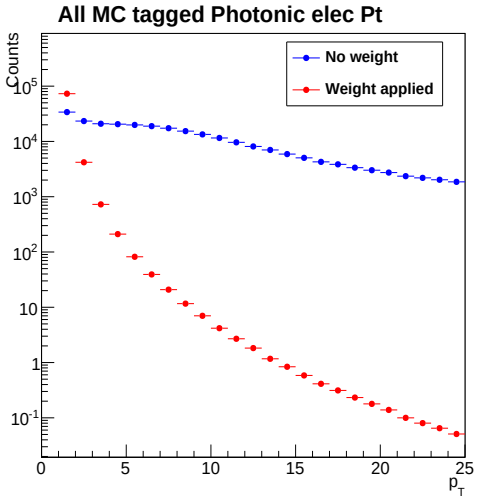

Figure 19: p_{T} distribution of electrons before and after applying the weights.

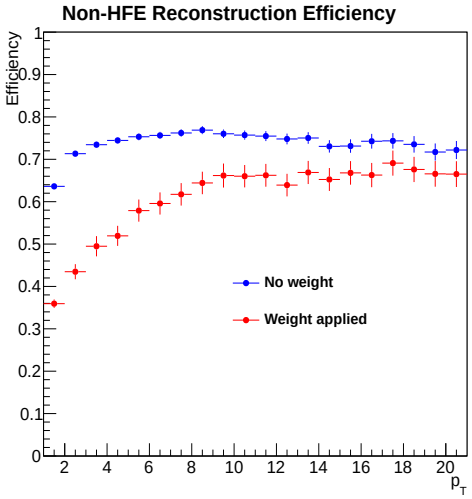

Figure 20: Non-HFE reconstruction efficiency as a function of $p_{\mathrm{T}}^{\mathrm{e}}$ before and after applying the weights.

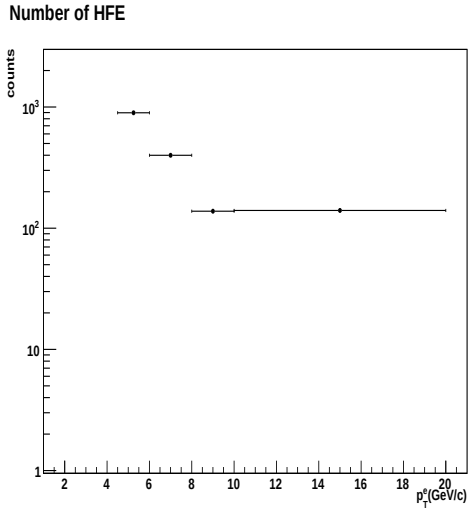

Figure 21: Heavy flavour decay electron raw yield as a function of p_{T} bins for semi-central Pb-Pb collisions.

6 Azimuthal angular correlations between heavy flavour electrons and charged hadrons

The azimuthal angular correlation between heavy flavour decay electrons and charged hadrons in two different hadron p_{T} bins, $2 < p_{\mathrm{T}}^{\mathrm{h}} < 4$ GeV/c and $4 < p_{\mathrm{T}}^{\mathrm{h}} < 6$ GeV/c is calculated with

$$\frac{dN^{HF}}{d\Delta\phi_{e-h}} = \frac{dN^{Incl}}{d\Delta\phi_{e-h}} - \frac{dN^{NHF-reco}}{d\Delta\phi_{e-h}} - \left(\frac{1}{\epsilon^{NHFE}} - 1\right)\frac{dN^{NHF-NoPartner}}{d\Delta\phi_{e-h}}, \tag{10}$$

where each of the angular correlation distributions on the right hand side of the equation is experimentally determined. In this calculation hadron contamination is removed by subtracting $\frac{dN^{h-h}}{d\Delta\phi_{e-h}}$ from $\frac{dN^{Incl}}{d\Delta\phi_{e-h}}$ (see figures 22 and 23). Both reconstructed and not-reconstructed $\frac{dN^{NHF}}{d\Delta\phi_{e-h}}$ are obtained from equation 11 (see figures 24, 25, 26 and 27). The $\frac{dN^{HF}}{d\Delta\phi_{e-h}}$ is obtained from equation 10 which is shown in figures 28 and 29.

$$\frac{dN^{NHF}}{d\Delta\phi_{e-h}} = \frac{dN^{ULS}}{d\Delta\phi_{e-h}} - \frac{dN^{LS}}{d\Delta\phi_{e-h}}, \tag{11}$$

Hadron tracks are selected by selecting AOD tracks which pass the filter mask `AliAODTrack::kTrkTPCOnly`. Additional cuts applied are shown in table 4.

Table 4: Track selection cuts for hadrons

Track property	Cut applied
Min number of TPC clusters	80
ITS and TPC refit	yes
Pseudorapidity	$-0.9 < \eta < 0.9$
p_{T}	$< p_{\mathrm{T}}^{\mathrm{e}}$

The distribution for $\frac{dN^{NHF-notreco}}{d\Delta\phi_{e-h}}$ is calculated from the azimuthal angular correlation between non-HFE and hadrons ($\frac{dN^{NHF-reco}}{d\Delta\phi_{e-h}}$). Since the not-reconstructed Non-HFE misses its partner electron in the reconstruction of Non-HFE, we remove the partner electron from $\frac{dN^{NHF-notreco}}{d\Delta\phi_{e-h}}$ and correct with the reconstruction efficiency ($\frac{1}{\epsilon^{NHFE}}-1$) to calculate $\frac{dN^{NHF-notreco}}{d\Delta\phi_{e-h}}$.

6.1 Mixed event correction

The azimuthal angular correlation function can be affected by any possible acceptance and detector effects. This bias can be removed using mixed event correlations. In this technique a pool of hadrons from different events are created. The hadron tracks are applied with the same cuts as in the analysis for same event. The pool is divided into 5 bins in centrality and 5 bins in primary vertex position along z axis. A minimum of 5 events are required to build the mixed event correlation. The electrons from one event are correlated with hadrons in the pool. It is also required that the pool does not contain hadrons from the same event.

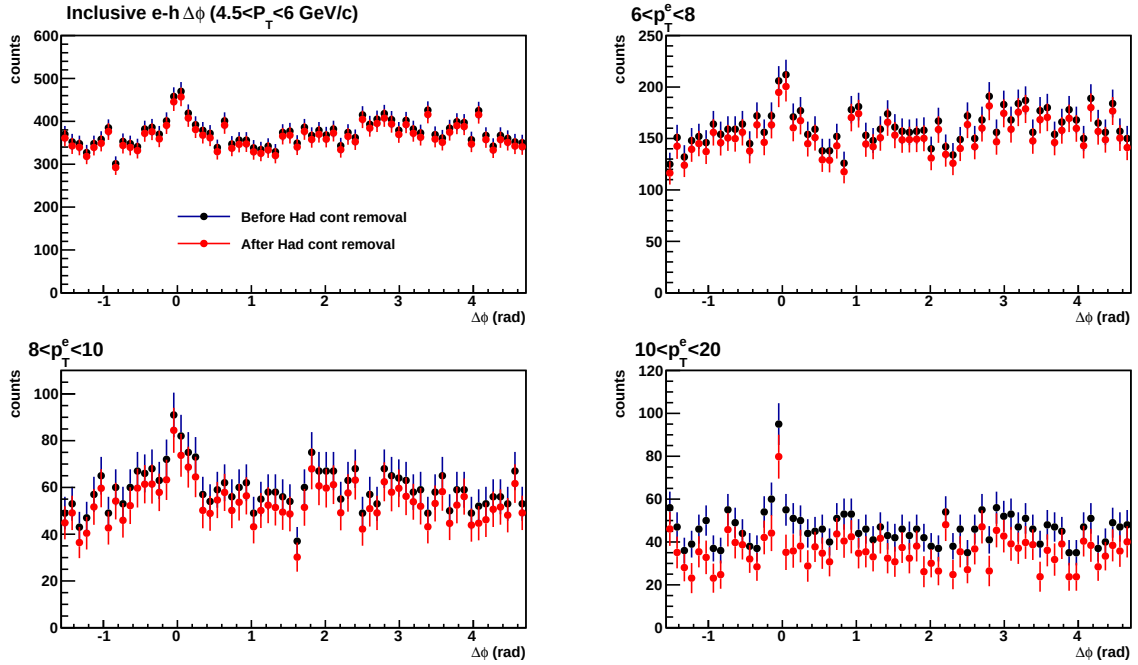

Figure 22: Azimuthal angular correlation between electrons and charged hadrons before and after hadron contamination removal for $2 < p_{\mathrm{T}}^{\mathrm{h}} < 4$ GeV/c in 4 $p_{\mathrm{T}}^{\mathrm{e}}$ bins from 4.5 to 20 GeV/c for semi-central Pb-Pb collisions.

The resulting correlation distribution between heavy flavour decay electrons and charged hadrons is normalised with number of entries at $\Delta\phi \approx 0$ ($\beta : N^{\Delta\phi=0}$). Since we are interested only in the $\Delta\phi$ distribution, mixed event is taken only in $\Delta\phi$ instead of ($\Delta\phi$, $\Delta\eta$).

The bias in the $\Delta\phi$ correlation function from detector effects is corrected for by taking the ratio of $\frac{dN^{SE}}{d\Delta\phi_{HFe-h}}$ and $\frac{dN^{ME}}{d\Delta\phi_{HFe-h}}$ as in Equation 12 (see figures 30 and 31).

$$\frac{dN^{SE-corr}}{d\Delta\phi_{HFe-h}} = \frac{\frac{dN^{SE}}{d\Delta\phi_{HFe-h}}}{\frac{dN^{ME}}{d\Delta\phi_{HFe-h}}/\beta} \tag{12}$$

6.2 Efficiency correction for hadrons

The aim of this analysis is to calculate the yield of associated hadrons per trigger electron. This requires efficiency correction to be applied on the hadrons. Since the analysis is done normalising with trigger electrons and the efficiency of reconstruction of electrons is expected to be flat, we do not apply the electron reconstruction efficiency.

The tracking efficiency for hadrons is calculated using the MC sample `LHC12a17e_fix` for $20 - 50\%$ central events. The efficiency is defined as the ratio of reconstructed tracks after hadron selection cuts (setting: *Is physical primary*) to all physical primary tracks in the MC stack. The plot of the tracking efficiency is shown in figure 32.

Other corrections for hadrons like p_{T} resolution are negligible and not applied.

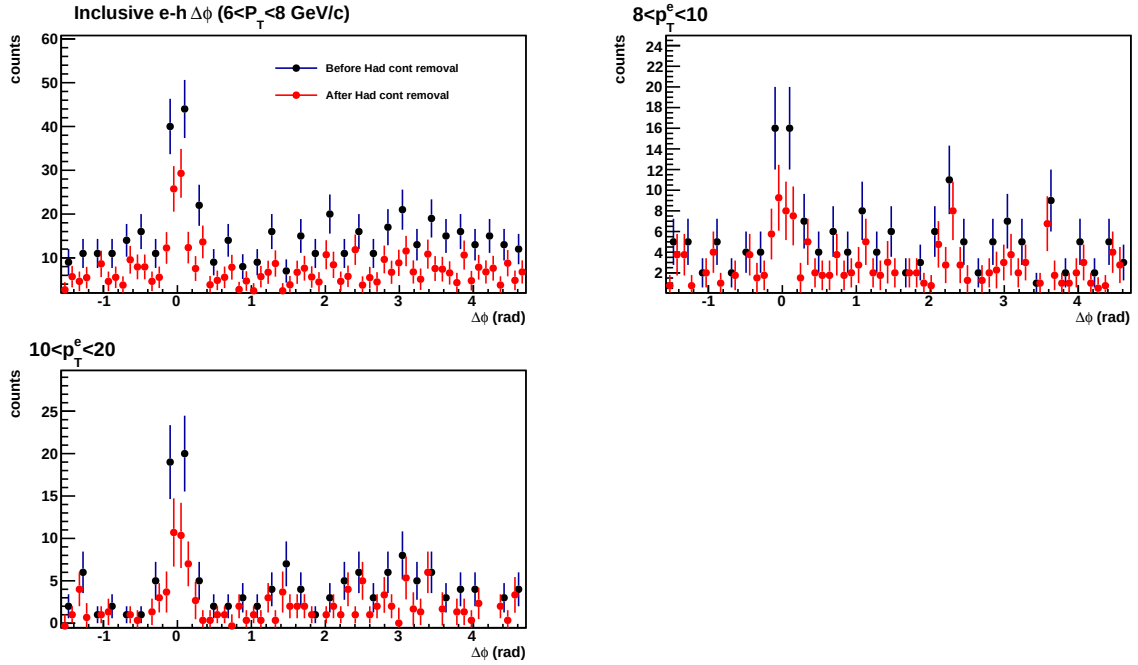

Figure 23: Azimuthal angular correlation between electrons and charged hadrons before and after hadron contamination removal for $4 < p_{\mathrm{T}}^{\mathrm{h}} < 6$ GeV/c in 3 $p_{\mathrm{T}}^{\mathrm{e}}$ bins from 6 to 20 GeV/c for semi-central Pb-Pb collisions.

6.3 Flow contribution

The azimuthal angular correlation between heavy flavour decay electrons and charged hadrons have contributions from uncorrelated pair of particles (which is expected to be flat), from jet fragmentation and from flow of heavy flavour decay electrons and charged hadrons. The main flow contribution comes from the second component of fourier series (v_2). The flow contribution in the $\Delta\phi$ distribution is estimated using:

$$2v_2^{trig}v_2^{asso}cos(2\Delta\phi), \tag{13}$$

where the value of v_2^{trig} and v_2^{asso} are obtained from ALICE measurements [30]. The v_2 of electrons and hadrons measured is shown in figure 33.

Since v_2 of hadrons is measured in finer centrality and p_{T} bins, we combine the centrality and p_{T} as weighted mean to match with this analysis as below where σ^{stat} (σ^{sys}) is the statistical (systematic) error:

$$v_2^{combined} = \frac{\sum_i (v_2^i/\sigma^2_{v_2^i})}{\sum_i (1/\sigma^2_{v_2^i})}, \tag{14}$$

$$\sigma^{stat}_{v_2^{combined}} = \frac{\sum_i (\sigma^{stat}_{v_2^i}/\sigma^2_{v_2^i})}{\sum_i (1/\sigma^2_{v_2^i})}, \tag{15}$$

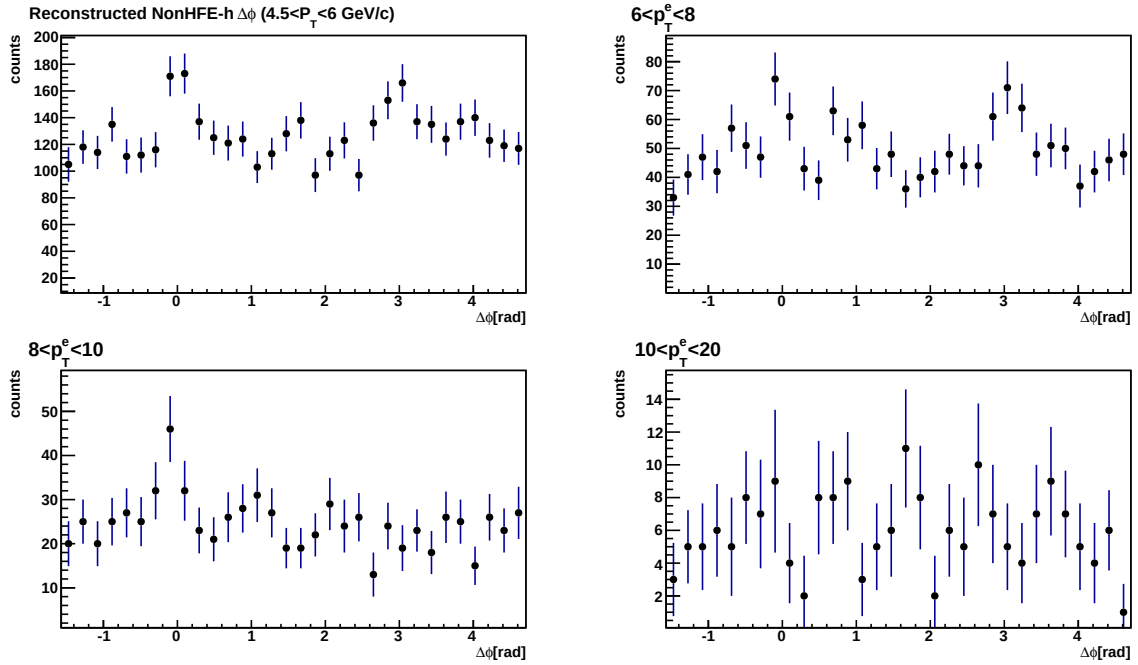

Figure 24: Azimuthal angular correlation between reconstructed Non-HFE and charged hadrons ($\frac{dN^{ULS}}{d\Delta\phi_{e-h}} - \frac{dN^{LS}}{d\Delta\phi_{e-h}}$) for $2 < p_{\mathrm{T}}^{\mathrm{h}} < 4$ GeV/c in 4 $p_{\mathrm{T}}^{\mathrm{e}}$ bins from 4.5 to 20 GeV/c for semi-central Pb-Pb collisions.

$$\sigma^{sys}_{v_2^{combined}} = \frac{\sum_i (\sigma^{sys}_{v_2^i} / \sigma^2_{v_2^i})}{\sum_i (1/\sigma^2_{v_2^i})}, \tag{16}$$

$$(\sigma_{v_2^i})^2 = (\sigma^{stat}_{v_2^i})^2 + (\sigma^{sys}_{v_2^i})^2, \tag{17}$$

where i represents points to be summed over (see figure 34) [31].

Since the only available v_2 of electrons is for $20-40\%$ centrality, this value is considered to estimate the flow contribution in this analysis. This estimate gives the approximate value for $20-50\%$ central events.

The flow contribution in the $\frac{dN}{d\Delta\phi_{HFe-h}}$ for $20-50\%$ central events is shown in figure 35 and 36.

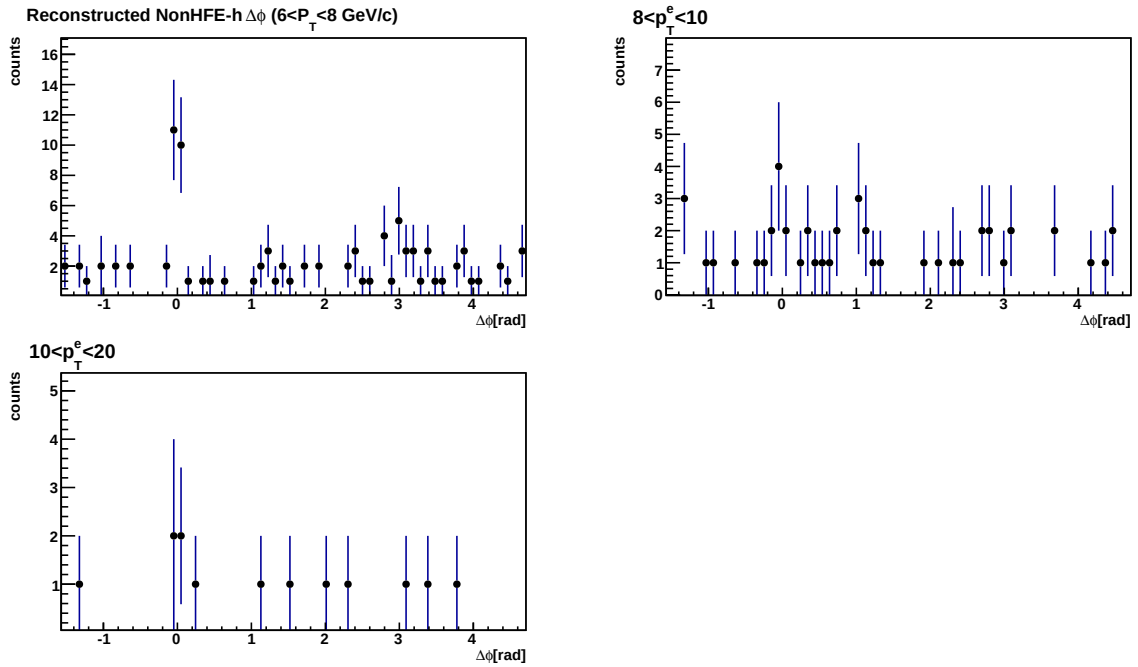

Figure 25: Azimuthal angular correlation between reconstructed Non-HFE and charged hadrons ($\frac{dN^{ULS}}{d\Delta\phi_{e-h}} - \frac{dN^{LS}}{d\Delta\phi_{e-h}}$) for $4 < p_{\mathrm{T}}^{\mathrm{h}} < 6$ GeV/c in 3 $p_{\mathrm{T}}^{\mathrm{e}}$ bins from 6 to 20 GeV/c for semi-central Pb-Pb collisions.

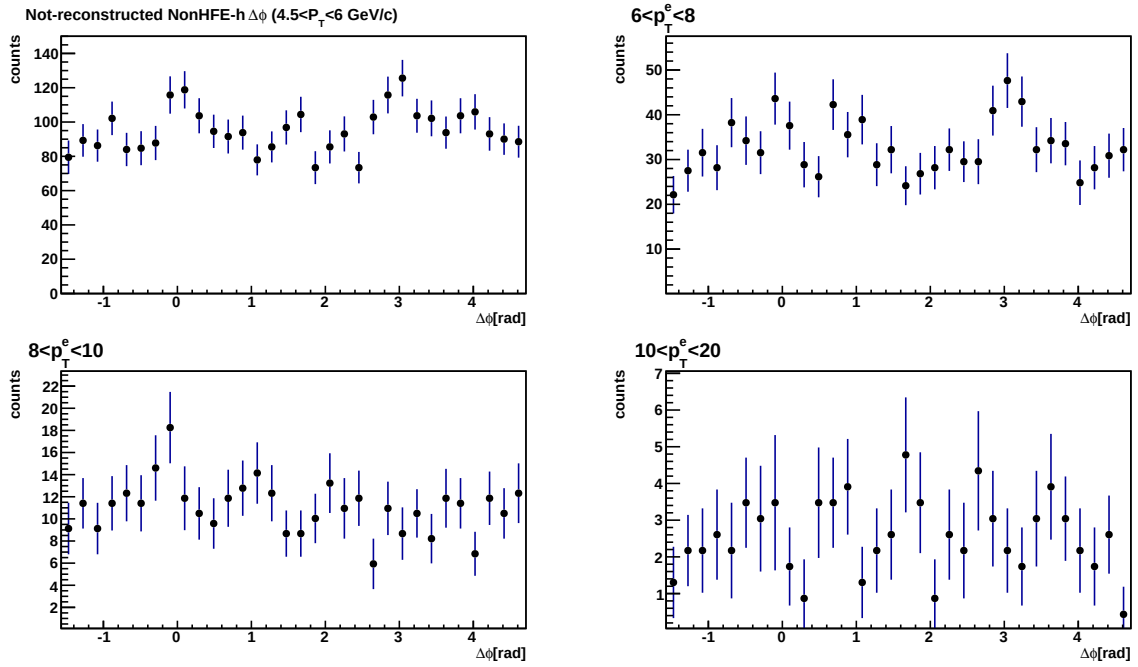

Figure 26: Azimuthal angular correlation between not reconstructed Non-HFE and charged hadrons ($\frac{dN^{ULS-nopartner}}{d\Delta\phi_{e-h}} - \frac{dN^{LS-nopartner}}{d\Delta\phi_{e-h}}$) for $2 < p_{\mathrm{T}}^{\mathrm{h}} < 4$ GeV/c in 4 $p_{\mathrm{T}}^{\mathrm{e}}$ bins from 4.5 to 20 GeV/c for semi-central Pb-Pb collisions.

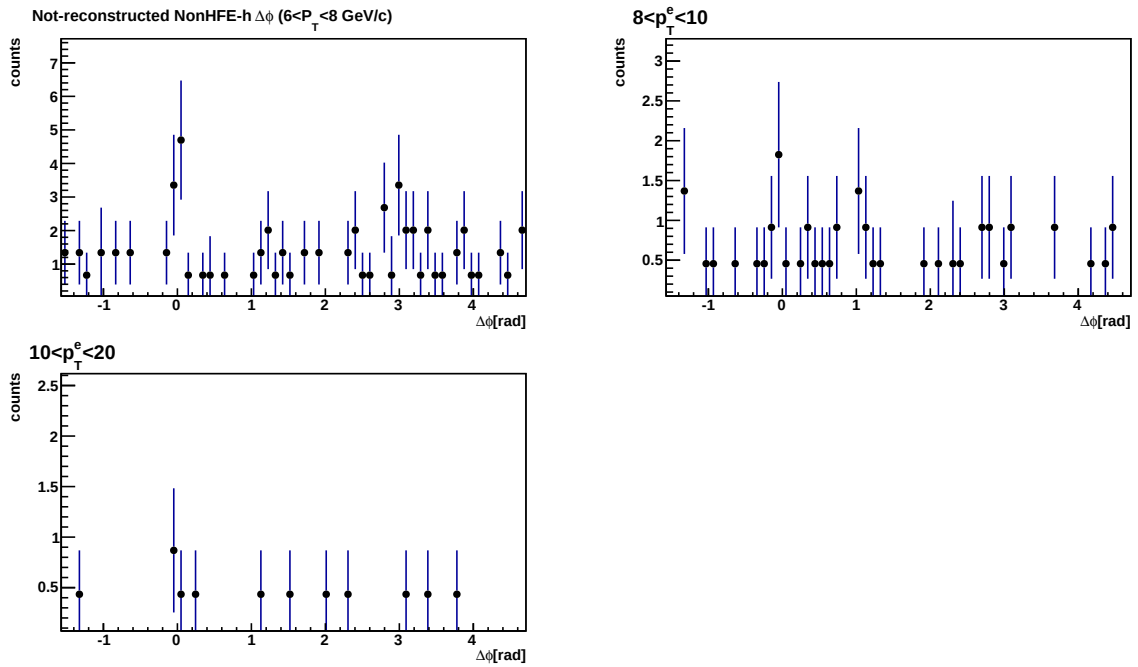

Figure 27: Azimuthal angular correlation between not reconstructed Non-HFE and charged hadrons ($\frac{dN^{ULS-nopartner}}{d\Delta\phi_{e-h}} - \frac{dN^{LS-nopartner}}{d\Delta\phi_{e-h}}$) for $4 < p_{\mathrm{T}}^{\mathrm{h}} < 6$ GeV/c in 3 $p_{\mathrm{T}}^{\mathrm{e}}$ bins from 6 to 20 GeV/c for semi-central Pb-Pb collisions.

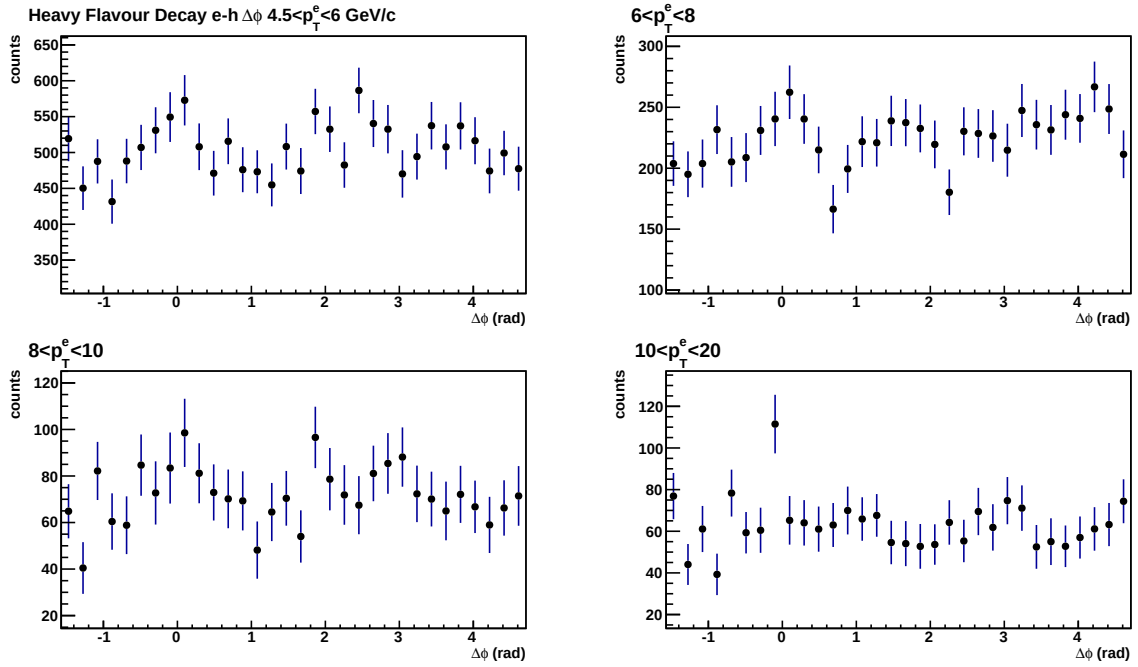

Figure 28: Azimuthal angular correlation between heavy flavour decay electrons and charged hadrons for $2 < p_{\mathrm{T}}^{\mathrm{h}} < 4$ GeV/c in 4 $p_{\mathrm{T}}^{\mathrm{e}}$ bins from 4.5 to 20 GeV/c for semi-central Pb-Pb collisions.

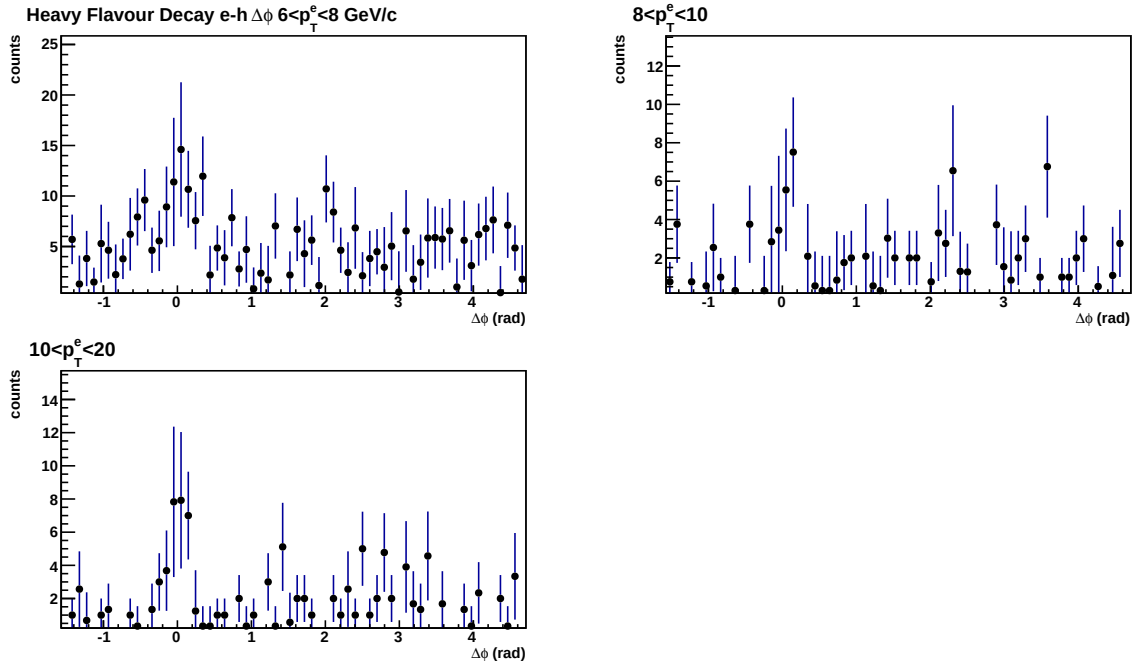

Figure 29: Azimuthal angular correlation between heavy flavour decay electrons and charged hadrons for $4 < p_{\mathrm{T}}^{\mathrm{h}} < 6$ GeV/c in 3 $p_{\mathrm{T}}^{\mathrm{e}}$ bins from 6 to 20 GeV/c for semi-central Pb-Pb collisions.

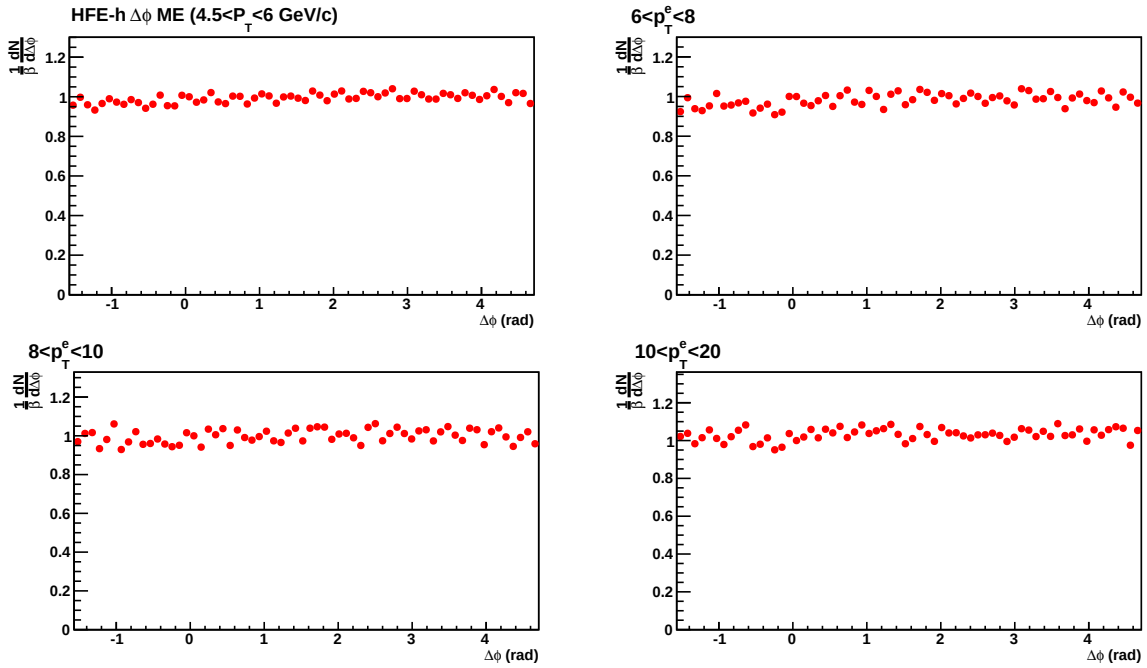

Figure 30: Mixed event azimuthal angular correlation between heavy flavour decay electrons and charged hadrons normalized by β ($N^{\Delta\phi=0}$) for $2 < p_{\mathrm{T}}^{\mathrm{h}} < 4$ GeV/c in 4 $p_{\mathrm{T}}^{\mathrm{e}}$ bins from 4.5 to 20 GeV/c for semi-central Pb-Pb collisions.

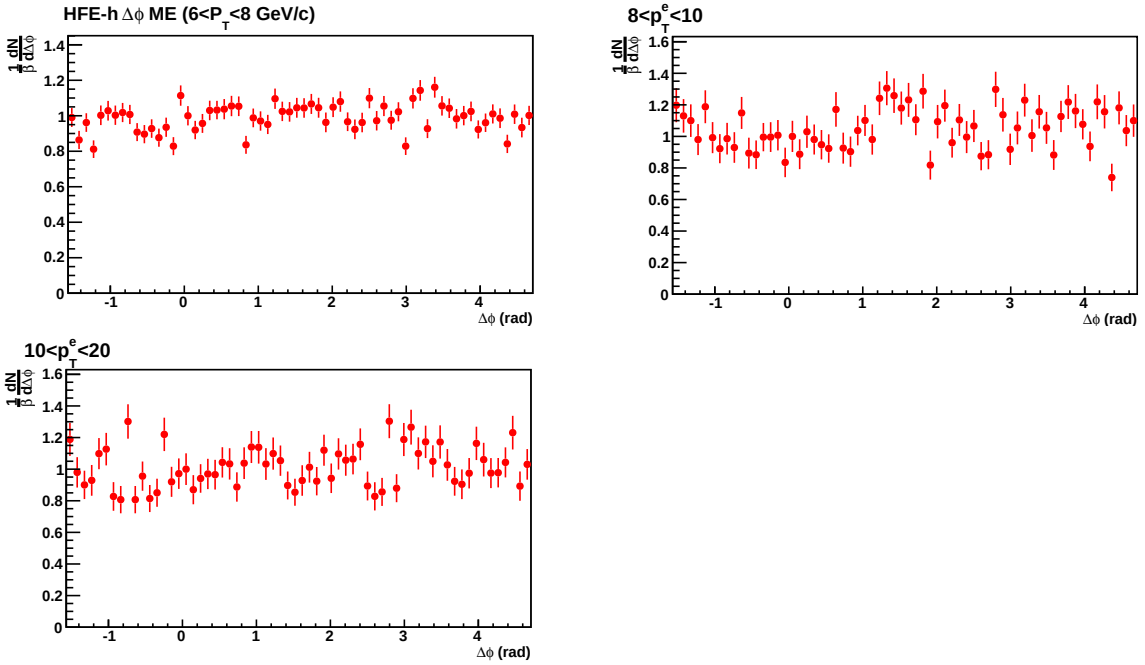

Figure 31: Mixed event azimuthal angular correlation between heavy flavour decay electrons and charged hadrons normalized by β ($N^{\Delta\phi=0}$) for $4 < p_{\mathrm{T}}^{\mathrm{h}} < 6$ GeV/c in 3 $p_{\mathrm{T}}^{\mathrm{e}}$ bins from 6 to 20 GeV/c for semi-central Pb-Pb collisions.

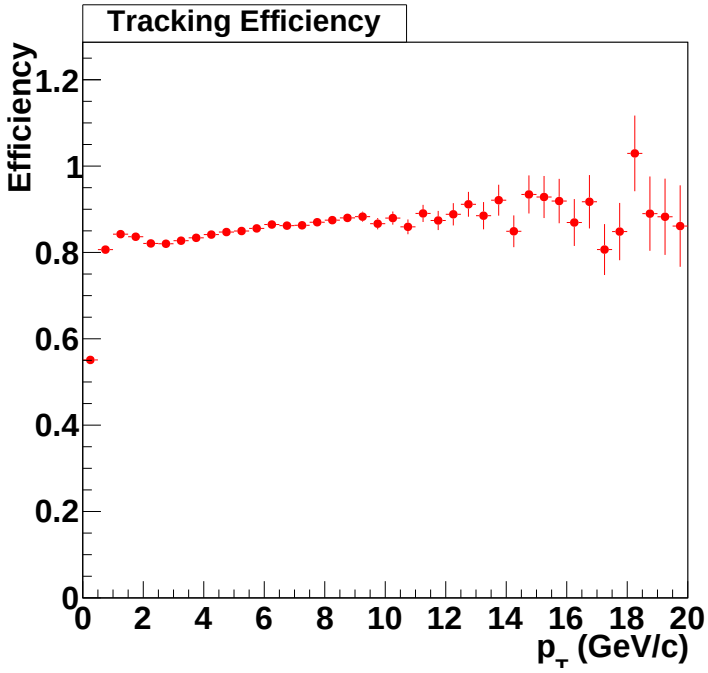

Figure 32: Tracking efficiency for hadrons.

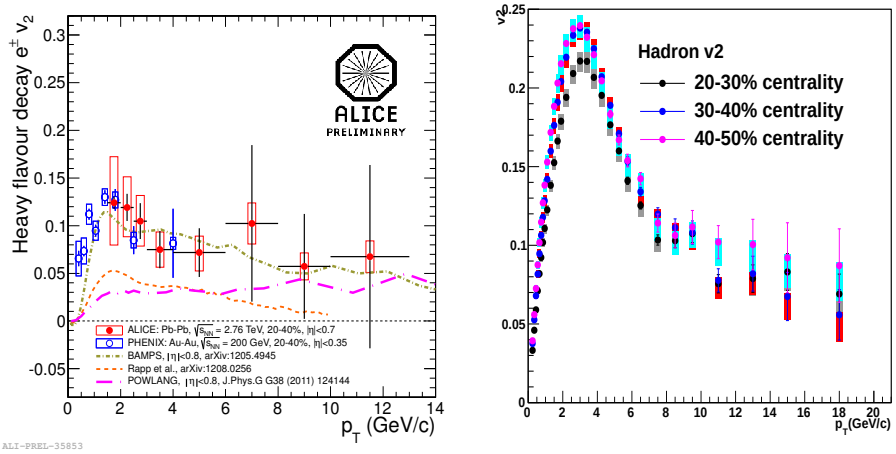

Figure 33: Elliptic flow parameter v_2 of electrons for $20-40\%$ (left panel) and hadrons for $20-50\%$ (right panel) centrality classes.

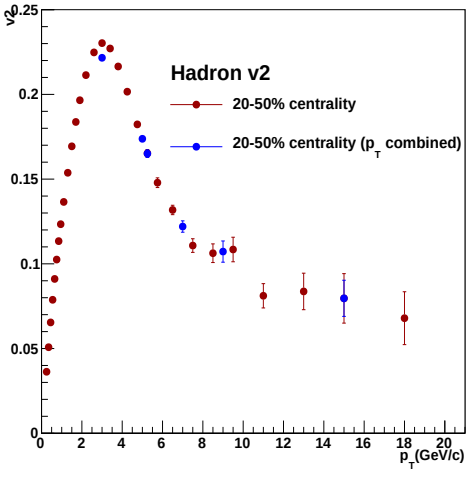

Figure 34: Combined values of v_2 of hadrons using Equations 15, 16 and 17.

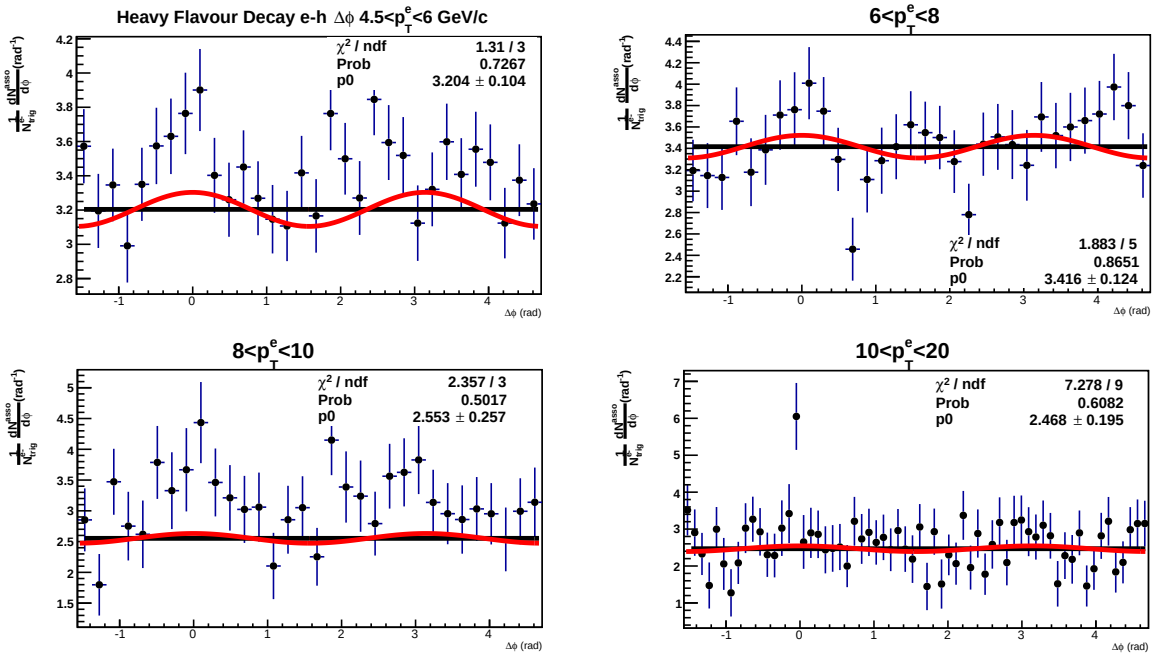

Figure 35: Azimuthal angular correlation between heavy flavour decay electrons and charged hadrons (normalised with bin width) with flow contribution (red curve) for $2 < p_{\mathrm{T}}^{\mathrm{h}} < 4$ GeV/c in 4 $p_{\mathrm{T}}^{\mathrm{e}}$ bins from 4.5 to 20 GeV/c for semi-central Pb-Pb collisions.

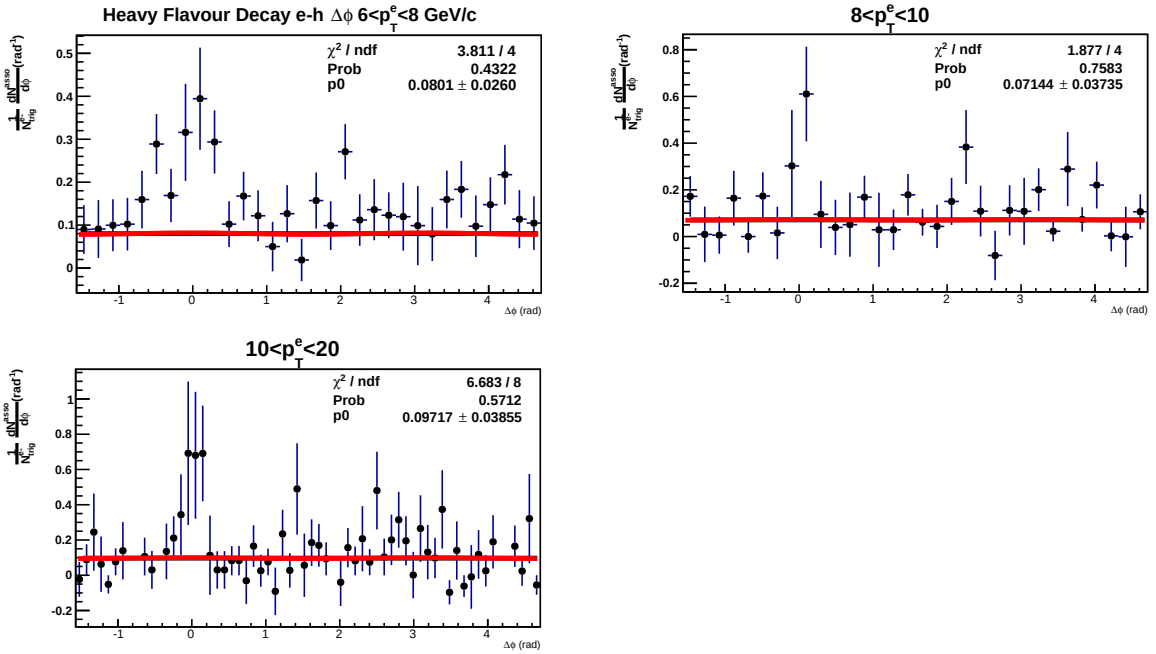

Figure 36: Azimuthal angular correlation between heavy flavour decay electrons and charged hadrons (normalised with bin width) with flow contribution (red curve) for $4 < p_{\mathrm{T}}^{\mathrm{h}} < 6$ GeV/c in 3 $p_{\mathrm{T}}^{\mathrm{e}}$ bins from 6 to 20 GeV/c for semi-central Pb-Pb collisions.

6.4 Near-side yield and width

The near-side yield and width of the azimuthal angular correlation between heavy flavour decay electrons and charged hadrons is obtained by fitting the $\frac{1}{\sqrt{2\pi\sigma^2}}\exp\left(-\frac{(x-\mu)^2}{2\sigma^2}\right) + pol0 * (1 + 2v_2^e v_2^h cos(2\Delta\phi))$ for $20-50\%$ central Pb-Pb events on the near-side as shown in figures 37 and 38.

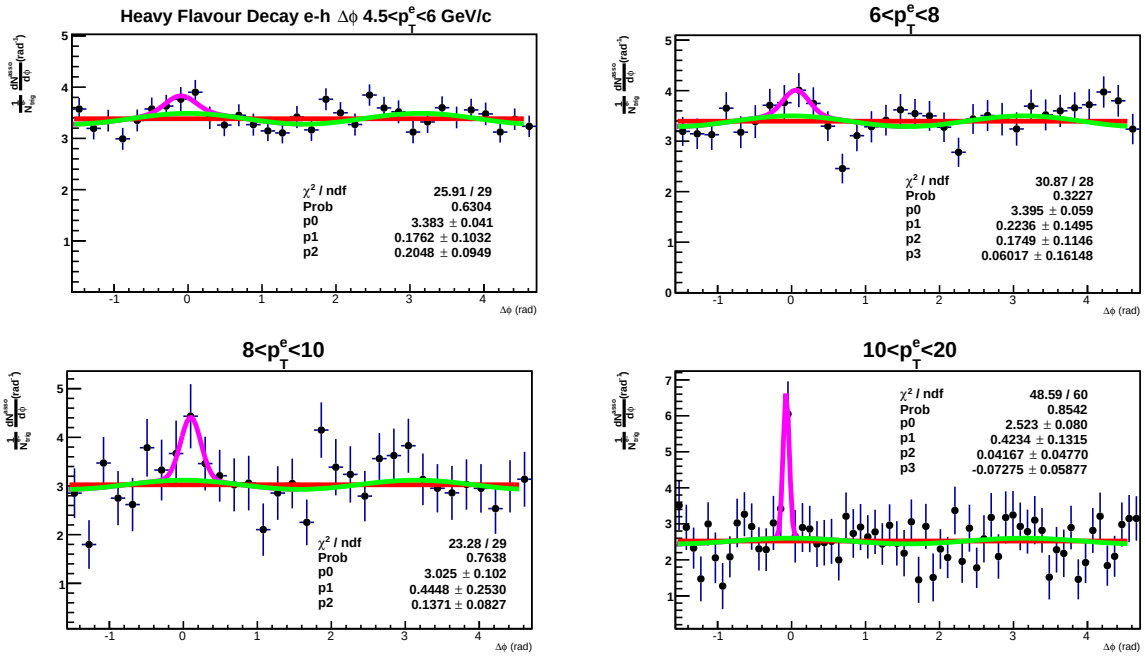

Figure 37: Azimuthal angular correlation between heavy flavour decay electrons and charged hadrons (normalised with bin width) fitted with the function $Gaus(0) + pol0 * (1 + 2v_2^e v_2^h cos(2\Delta\phi))$, for $2 < p_{\mathrm{T}}^{\mathrm{h}} < 4$ GeV/c in 4 $p_{\mathrm{T}}^{\mathrm{e}}$ bins from 4.5 to 20 GeV/c for semi-central Pb-Pb collisions.

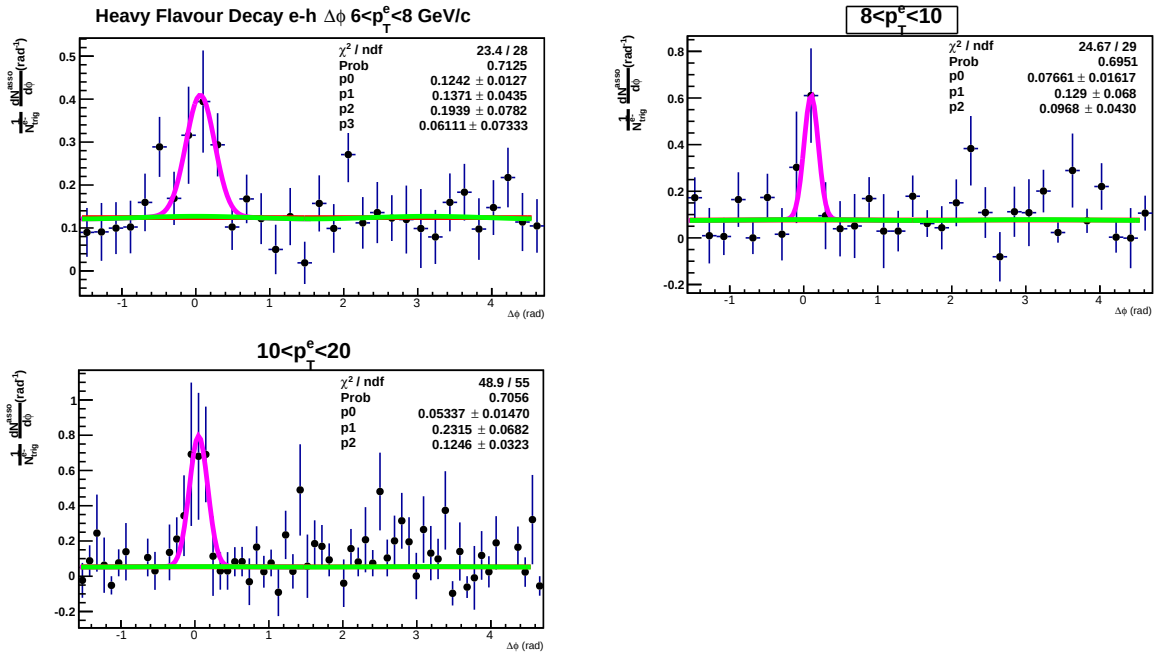

Figure 38: Azimuthal angular correlation between heavy flavour decay electrons and charged hadrons (normalised with bin width) fitted with the function $Gaus(0) + pol0 * (1 + 2v_2^e v_2^h cos(2\Delta\phi))$, for $4 < p_{\mathrm{T}}^{\mathrm{h}} < 6$ GeV/c in 3 $p_{\mathrm{T}}^{\mathrm{e}}$ bins from 6 to 20 GeV/c for semi-central Pb-Pb collisions.

The yield and width obtained from the fit for semi-central Pb-Pb collisions for two different $p_{\mathrm{T}}^{\mathrm{h}}$ bins are shown in figures 39 and 40.

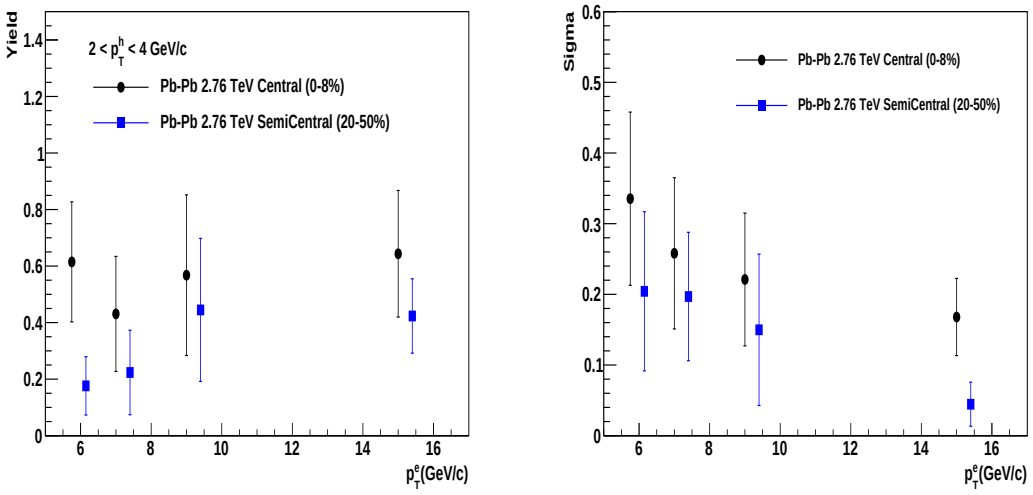

Figure 39: The near-side yield (left panel) and width (right panel) obtained from the fit for most central and semi-central events for $2 < p_{\mathrm{T}}^{\mathrm{h}} < 4$ GeV/c as a function of $p_{\mathrm{T}}^{\mathrm{e}}$.

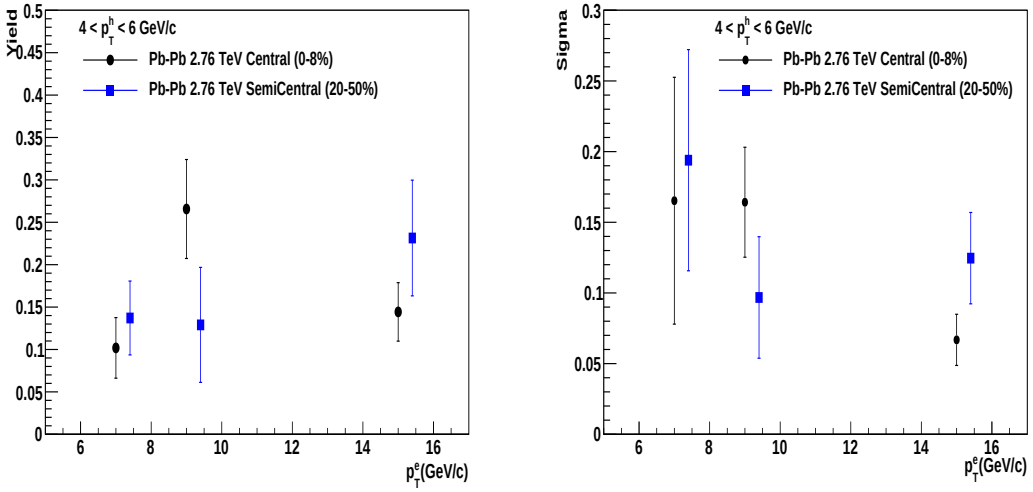

Figure 40: The near side yield (left panel) and width (right panel) obtained from the fit for semi-central event for $4 < p_{\mathrm{T}}^{\mathrm{h}} < 6$ GeV/c as a function of $p_{\mathrm{T}}^{\mathrm{e}}$.

7 Systematics

The systematical uncertainties were estimated by changing the cut parameters used for the track selection, the efficiency estimation, flow contribution and for the fit.

The following systematic error study is performed on the yield from the fit.

1. Electron identification cuts
   - $\sigma_{\mathrm{TPC-d}E/\mathrm{d}x}$ cut value
   - E/p cut value
   - Shower shape cut values (M02 and M20)
2. Electron track cuts
   - TPC number of clusters
3. Hadron track cuts
   - TPC number of clusters
   - Statistical error on tracking efficiency
   - Weak and secondary decay contamination
4. Non-HFE estimation
   - Invariant mass cut
   - TPC number of clusters for associated track
   - No ITS refit on associated track
   - Invariant mass calculation method
5. Fit parameters
   - Fix mean
   - Pedestal values
   - Bin counting
6. Flow estimation

7.1 Error propagation methods

7.1.1 Poisson method

The Poisson error propagation method, which is also refered as general error propagation method is proper for the cases where there is no correlation between the measured quantities. The uncertainty in a quantity $q = f(x, y)$ which is an arbitrary function of measured quantities x and y is also a function of the measured quantities and their associated uncertainties. If all these measured quantities are uncorrelated or in other words the errors Δx and Δy

are independent and random then these errors tend to partially cancel and a more realistic determination of the uncertainty in q is obtained by evaluating the partial derivatives and then adding the errors in quadrature [34].

$$\delta \mathrm{q} = \sqrt{(\frac{\partial \mathrm{q}}{\partial \mathrm{x}} \Delta \mathrm{x})^2 + (\frac{\partial \mathrm{q}}{\partial \mathrm{y}} \Delta \mathrm{y})^2} \tag{18}$$

Since in this analysis the measured quantities are correlated, this error propagations is not used or systematic studies and instead the binomial error propagation method is used which is explained in 7.1.2.

7.1.2 Binomial method

This calculation is based on the knowledge that an application of a cut can be considered as a binomial process, where $q = k/N$ is the probability of success, and the standard deviation of the distribution of the number of events passing is

$$\sigma_k = \sqrt{var(k)} = \sqrt{q(1-q)N}. \tag{19}$$

The error on N will be equal to 0. Thus

$$\delta q = \frac{\delta k}{N} - \frac{k \delta N}{N^2} = \frac{\delta k}{N}. \tag{20}$$

Since we do not know the true propability of success [35], what is often done is to estimate q with q' and put it into this equation and then to divide through by N, yielding the result $\delta q' = \frac{1}{N}\sqrt{k(1-\frac{k}{N})}$ [35].

In this analysis, the new cuts used for the systematic uncertainties are subsets of the default cuts and thus calculated by binomial error propagation method.

7.2 Systematics uncertainities

The systematic uncertainties for different error sources are shown in figures 41-47. Table 5 gives the default cut and the varied values for the analysis. Table 6 gives uncertainity assigned to each systematic variables.

The total systematics is calculated by summing up the systematical uncertainties of each parameter in quadrature.

Error source	Default	Cut variation(loose)	Cut variation(tight)
$\sigma_{\mathrm{TPC-d}E/\mathrm{d}x}$	(-1,3)	(-1.5,3.5)	(-0.5,2.5)
E/p	(0.8,1.2)	(0.75,1.2)	(0.9,1.2)
Shower shape (M02)	(0.03,0.5)	(0.025,0.6)	(0.035,0.45)
Shower shape (M20)	(0.04,0.3)	(0.03,0.4)	(0.045,0.25)
TPC N clusters (Ele track)	100	90	110
TPC N clusters (Had track)	80	70	90
Weak decay contribution	-	5%	-
Invariant mass (MeV/c^2)	100	90	110
TPC N clusters (Asso ele track)	80	70	90
ITS refit	with refit	no refit	-
TPC N clusters (Asso ele track)	80	70	90
Flow Contribution	ref	ref-error	ref+error
Tracking Efficiency	ref	ref-error	ref+error
Bin counting	fit	-	
Fit parameters: fixing pedestal value	-	-	
Fit parameters: fixing mean value	-	-	

Table 5: List of variables used for the systematic uncertainties estimation and cut variation.

	$2 < p_{\mathrm{T}}^{\mathrm{h}} < 4$ GeV/c				$4 < p_{\mathrm{T}}^{\mathrm{h}} < 6$ GeV/c		
$p_{\mathrm{T}}^{\mathrm{e}}$ (GeV/c)	4.5-6	6-8	8-10	10-20	6-8	8-10	10-20
EID	15%	10%	10%	10%	10%	10%	10%
Non-HFE reco	15%	10%	10%	5%	15%	10%	5%
Fit	10%	10%	10%	5%	10%	10%	10%
Had TPC N clusters	10%	10%	10%	10%	7%	7%	7%
Weak decay contribution	3%	3%	3%	3%	3%	3%	3%
Tracking Efficiency	1%	1%	1%	1%	1%	1%	1%
Flow contribution	7%	7%	3%	0%	1%	0%	0%
Total	26%	21%	20%	16%	22%	19%	17%

Table 6: Systematic uncertainties for different error sources.

7.3 Systematic error evaluation for semi-central analysis

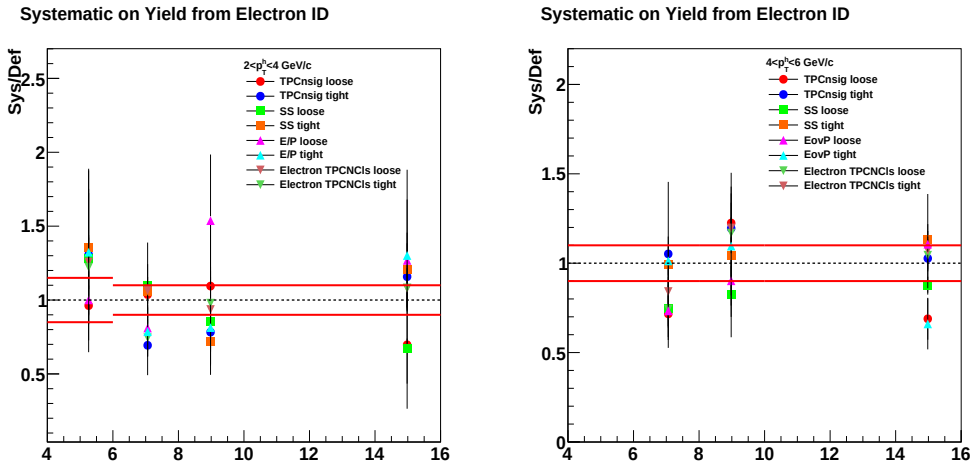

Figure 41: Systematics on electron identification for 2 $< p_{\mathrm{T}}^{\mathrm{h}} <$ 4 GeV/c (left panel) and 4 $< p_{\mathrm{T}}^{\mathrm{h}} <$ 6 GeV/c (right panel). Horizontal red lines are estimated from the central points of the systematics and represent the systematic error value assigned.

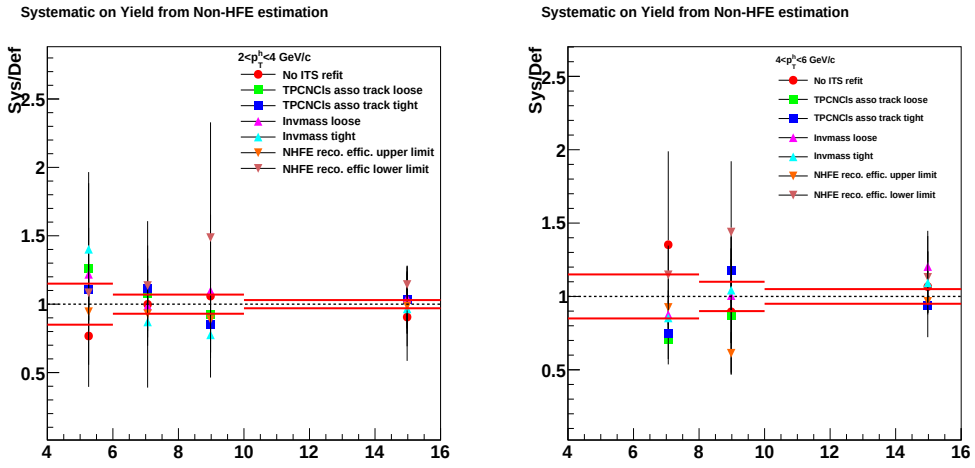

Figure 42: Systematics on Non-HFE reconstruction for 2 $< p_{\mathrm{T}}^{\mathrm{h}} <$ 4 GeV/c (left panel) and 4 $< p_{\mathrm{T}}^{\mathrm{h}} <$ 6 GeV/c (right panel). Horizontal red lines are estimated from the central points of the systematics and represent the systematic error value assigned.

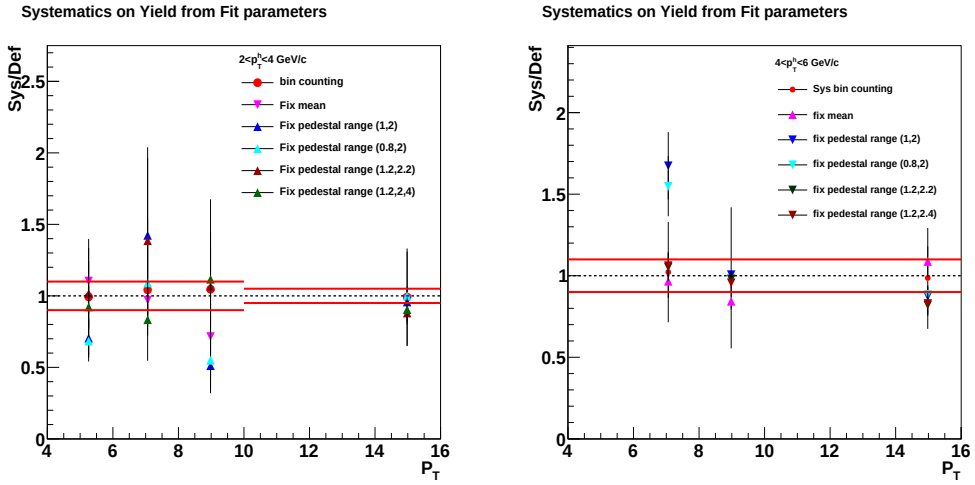

Figure 43: Systematics on fit parameters for 2 $<p_{\mathrm{T}}^{\mathrm{h}} <$ 4 GeV/c (left panel) and 4 $<p_{\mathrm{T}}^{\mathrm{h}} <$ 6 GeV/c (right panel). Horizontal red lines are estimated from the central points of the systematics and represent the systematic error value assigned.

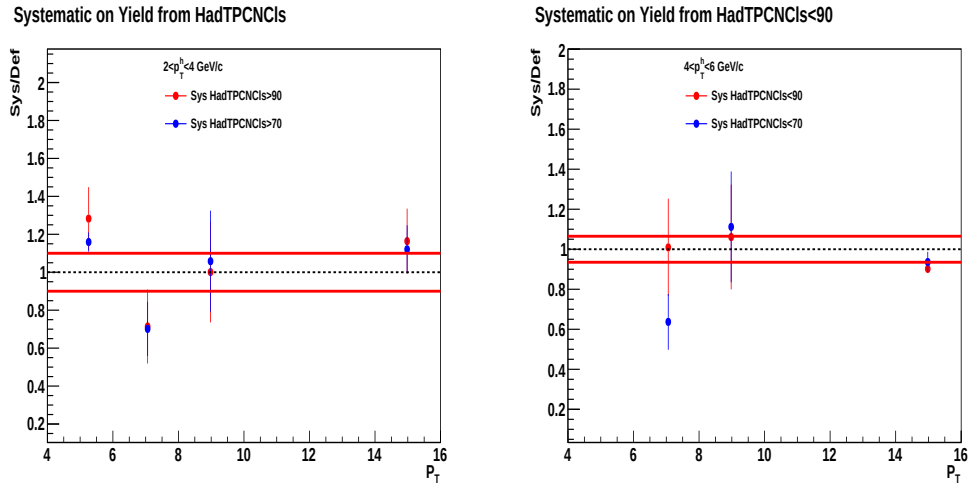

Figure 44: Systematics on minimum number of TPC clusters required for hadrons for 2 $<p_{\mathrm{T}}^{\mathrm{h}} <$ 4 GeV/c (left panel) and 4 $<p_{\mathrm{T}}^{\mathrm{h}} <$ 6 GeV/c (right panel). Horizontal red lines are estimated from the central points of the systematics and represent the systematic error value assigned.

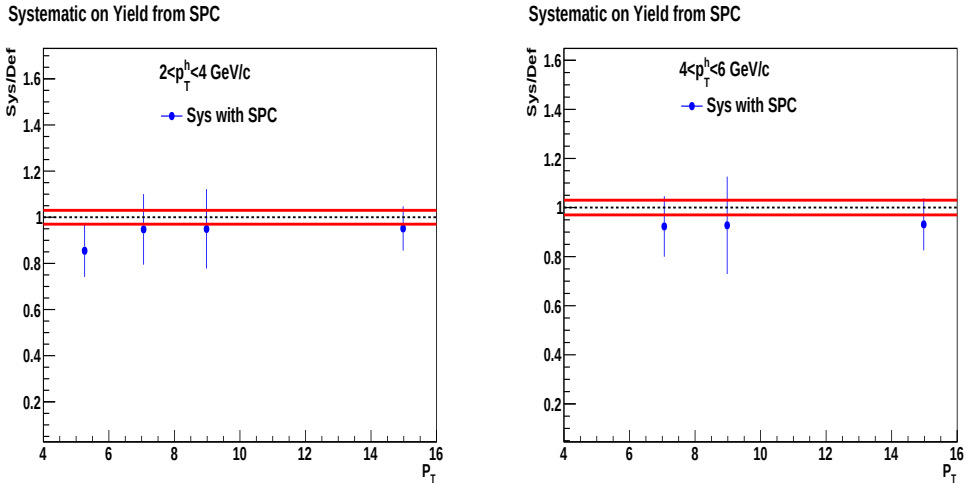

Figure 45: Systematics on yield by including secondary and weak decay correction for 2 $<p_{\mathrm{T}}^{\mathrm{h}}$ < 4 GeV/c (left panel) and 4 $<p_{\mathrm{T}}^{\mathrm{h}} < 6$ GeV/c (right panel). Horizontal red lines are estimated from the central points of the systematics and represent the systematic error value assigned.

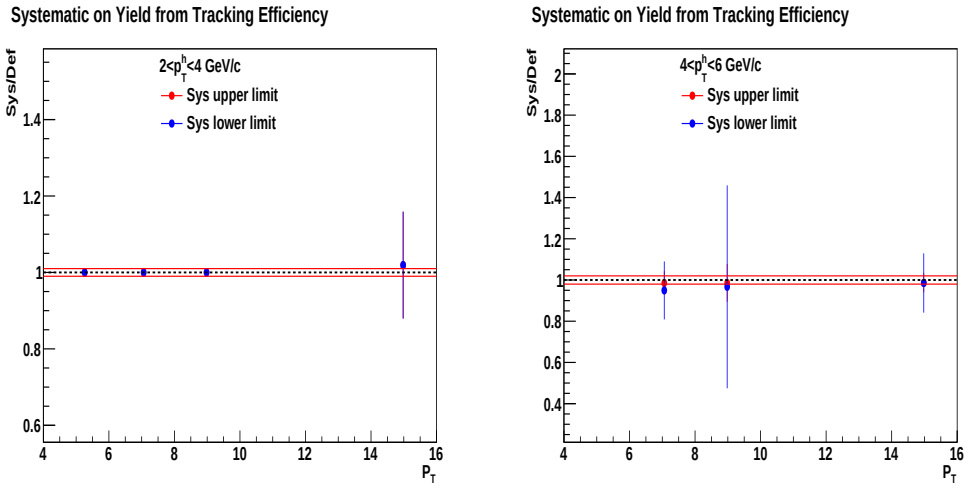

Figure 46: Systematics from statistical fluctuations on Tracking efficiency error for $2 < p_T^h < 4$ GeV/c (left panel) and $4 < p_T^h < 6$ GeV/c (right panel). Horizontal red lines are estimated from the central points of the systematics and represent the systematic error value assigned.

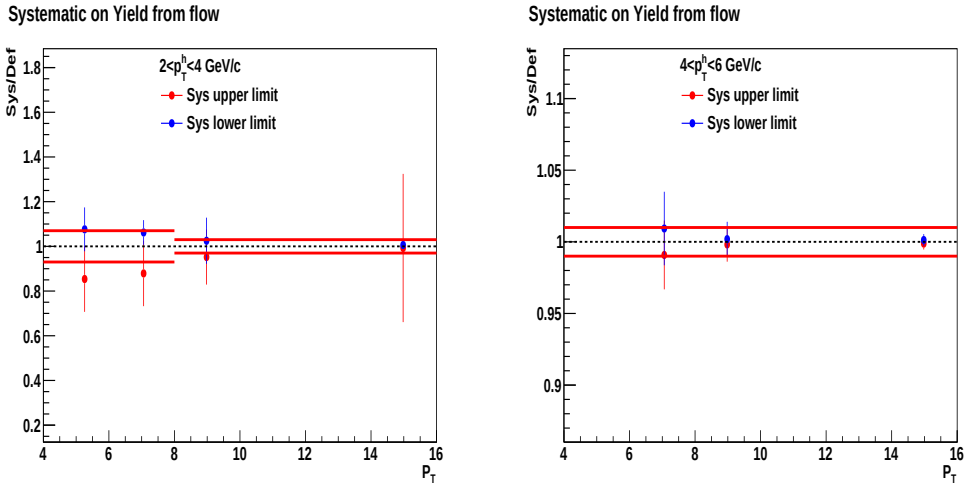

Figure 47: Systematics on electron flow contribution for $2 < p_T^h < 4$ GeV/c (left panel) and $4 < p_T^h < 6$ GeV/c (right panel). Horizontal red lines are estimated from the central points of the systematics and represent the systematic error value assigned.

8 Results

The near-side ($-\pi/2 < \frac{dN}{d\Delta\phi_{HFe-h}} < \pi/2$) yield is extracted from the azimuthal angular correlation distribution between heavy flavour decay electrons and charged hadrons in semi-central (20-50%) Pb-Pb collisions at $\sqrt{s_{\rm NN}} = 2.76$ TeV. The yield is compared to central (0-8%) Pb-Pb collisions [4] to measure possible modifications. It is also compared to pp collisions to study modification of fragmentation function in Pb-Pb collisions. The comparison is done to pp collisions at $\sqrt{s_{\rm NN}} = 7$ TeV [36] due to low statistics in pp collisions at $\sqrt{s_{\rm NN}} = 2.76$ TeV. The correlation yield and width from the 3 datasets are shown in figure 48 and 49 for $2 < p_{\rm T}^{\rm h} < 4$ GeV/c and $4 < p_{\rm T}^{\rm h} < 6$ GeV/c, respectively.

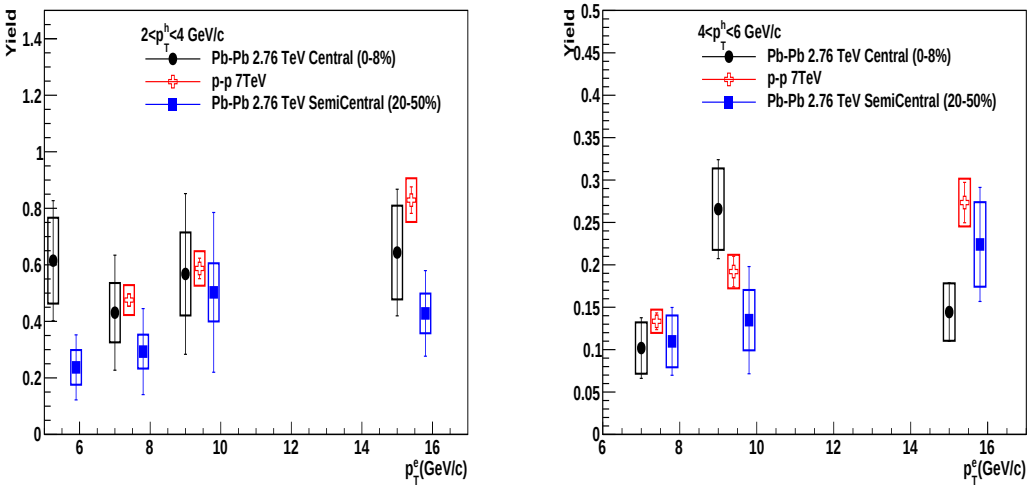

Figure 48: The near-side yield obtained from the fit for the central, semi-central Pb-Pb and pp analysis for $2 < p_{\rm T}^{\rm h} < 4$ GeV/c (left panel) and $4 < p_{\rm T}^{\rm h} < 6$ GeV/c (right panel) as a function of $p_{\rm T}^{\rm e}$.

The correlation yield from 3 datasets are compared by obtaining the ratio of yield in central to semi-central Pb-Pb collisions at $\sqrt{s_{\rm NN}} = 2.76$ ($I_{\rm CP}$) and semi-central (central) collisions (at $\sqrt{s_{\rm NN}} = 2.76$) to pp collisions at $\sqrt{s} = 7$ ($I_{\rm AA}$). $I_{\rm AA}$ is a probe to investigate the energy loss in the medium. $I_{\rm AA}$ also provides information about the jet fragmentation [37]. $I_{\rm CP}$ can be used to probe possible modifications.

8.1 Comparison of semi-central Pb-Pb collisions to pp 7 TeV

The ratio of the yield in semi-central Pb-Pb collisions at $\sqrt{s_{\rm NN}} = 2.76$ TeV to the one in pp collisions at $\sqrt{s} = 7$ TeV ($I_{\rm AA}$) is shown in figure 50.

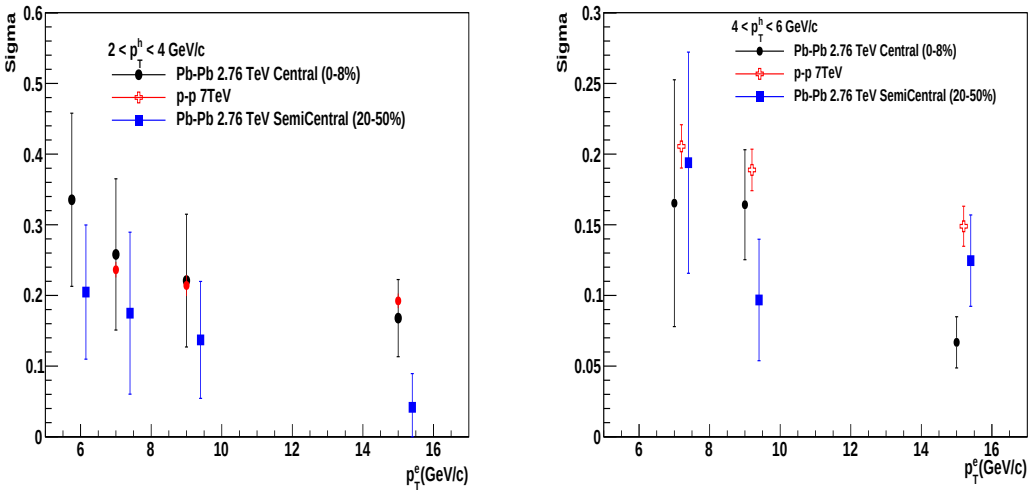

Figure 49: The near-side width obtained from the fit for the central, semi-central Pb-Pb and pp analysis for $2 < p_{\mathrm{T}}^{\mathrm{h}} < 4$ GeV/c (left panel) and $4 < p_{\mathrm{T}}^{\mathrm{h}} < 6$ GeV/c (right panel) as a function of $p_{\mathrm{T}}^{\mathrm{e}}$.

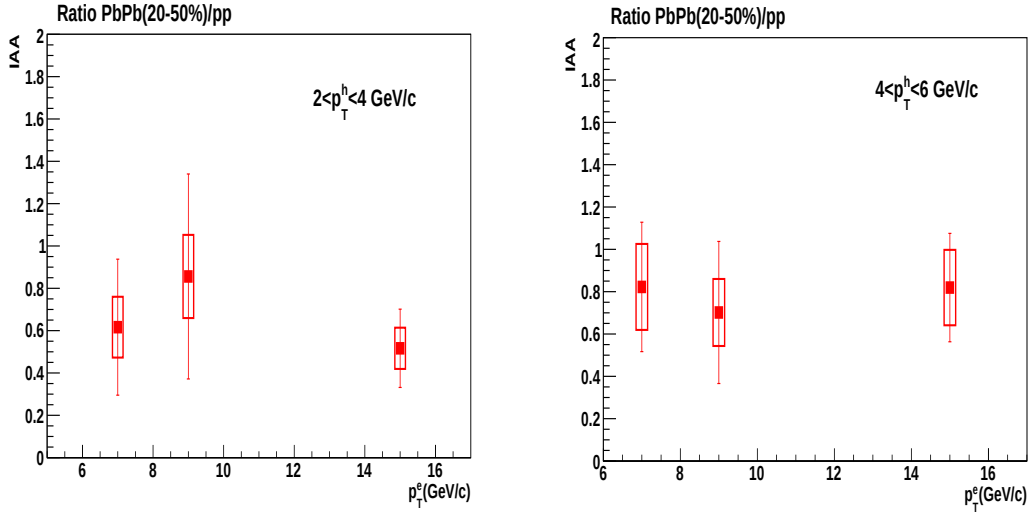

Figure 50: The ratio of yield in semi-central Pb-Pb collisions at 2.76 TeV to the yield in pp collisions at 7 TeV for $2 < p_{\mathrm{T}}^{\mathrm{h}} < 4$ GeV/c (left panel) and $4 < p_{\mathrm{T}}^{\mathrm{h}} < 6$ GeV/c (right panel) as a function of $p_{\mathrm{T}}^{\mathrm{e}}$.

8.2 Comparison of central to semi-central Pb-Pb collisions at 2.76 TeV

The ratio of yield in central to semi-central Pb-Pb collisions at 2.76 TeV (refered to as I_{CP}) is shown in figure 51.

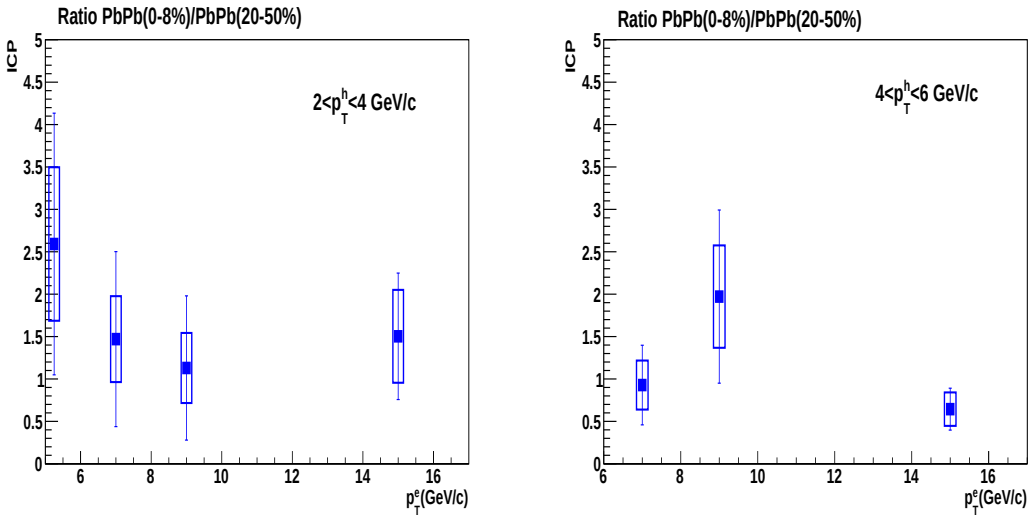

Figure 51: The ratio of yield in central to semi-central Pb-Pb collisions at 2.76 TeV for $2 < p_{\mathrm{T}}^{\mathrm{h}} < 4$ GeV/c (left panel) $4 < p_{\mathrm{T}}^{\mathrm{h}} < 6$ GeV/c (right panel) as a function of $p_{\mathrm{T}}^{\mathrm{e}}$.

8.3 Discussion

This analysis shows that the value of I_{AA} is smaller than 1. However within the statistical uncertainties ($\approx 40\%$) the value of I_{AA} is consistent with 1. There are indications that the I_{AA} does not show a $p_{\mathrm{T}}^{\mathrm{e}}$ dependence for both $2 < p_{\mathrm{T}}^{\mathrm{h}} < 4$ GeV/c and $4 < p_{\mathrm{T}}^{\mathrm{h}} < 6$ GeV/c [4]. The measurements of di-hadron correlations show a significant near-side enhancement of I_{AA} and a I_{AA} consistent with 1 [37].

The comparison of the I_{CP} in different $p_{\mathrm{T}}^{\mathrm{e}}$ bins indicates that the value of I_{CP} does not show a $p_{\mathrm{T}}^{\mathrm{e}}$ dependence. The value of the central points of the I_{CP} is higher than 1 for $2 < p_{\mathrm{T}}^{\mathrm{h}} < 4$ GeV/c and $4 < p_{\mathrm{T}}^{\mathrm{h}} < 6$ GeV/c, but within the error bars it is consistent with 1 [4]. The measurements of di-hadron correlations show a significant near-side enhancement of I_{CP} [37].

9 Conclusions and Outlook

The azimuthal angular correlation between heavy flavour decay electrons and charged hadrons are constructed in semi-central (20-50%) Pb-Pb collisions at $\sqrt{s_{\rm NN}} = 2.76$ TeV. The yield of the near side correlations ($-1 < \frac{dN}{d\Delta\phi_{HFe-h}} < 1$ rad) is extracted from a gaussion fit. The yield is compared between semi-central and central Pb-Pb collisions as well as to pp collisions at 7 TeV in two hadron $p_{\rm T}$ bins of $2 < p_{\rm T}^{\rm h} < 4$ GeV/c and $4 < p_{\rm T}^{\rm h} < 6$ GeV/c for heavy flavour decay electrons from 4.5 to 20 GeV/c.

The $I_{\rm AA}$, which is the ratio of hadron yield per trigger, is found to be ≈ 1.2 for light mesons. The $I_{\rm AA}$ in the heavy flavour sector with heavy flavour decay electron as trigger particle could yield a different value due to many factors. The fragmentation of b quarks is harder compared to c quarks giving lower hadron yield from parton shower. The heavy flavour electrons mainly come from the decay of D and B mesons. Different suppression factor ($R_{\rm AA}$) for D and B mesons are expected in Pb-Pb collisions, hence the relative contribution of electrons from D and B mesons is expected to be different in Pb-Pb collisions compared to pp. This affects the $I_{\rm AA}$ value on the near side.

In the present analysis, the value of $I_{\rm AA}$ is calculated and the central values are found to be smaller than 1, however due to large statistical uncertainity ($\approx 40\%$), $I_{\rm AA}$ values are consistent with 1.

To confirm any modification of the fragmentation function, we need to obtain smaller error bars on the yield and consequently on $I_{\rm AA}$. Therefore, more statistics for 2.76 TeV data is needed. This analysis can also be done by using the 5.02 TeV data in the future.

References

[1] Ch. Nattrass, System, energy, and flavor dependence of jets through di-hadron correlations in heavy ion collisions, PhD thesis, Yale University, 2009.

[2] D. Thomas et al, Azimuthal angular correlations of heavy flavour decay electrons and charged hadrons in proton-proton collisions at $\sqrt{s} = 2.76$ TeV using the ALICE detector (ALICE Analysis note), https://aliceinfo.cern.ch/Notes/node/130.

[3] ALICE Collaboration, The ALICE experiment at the CERN LHC, IOP Publishing Ltd and SISSA, JINST, 3 S, 08002 (2008).

[4] D. Thomas et al, Study of the azimuthal angular correlations between heavy flavour decay electrons and charged hadrons in lead–lead collisions at $\sqrt{s_{\mathrm{NN}}} = 2.76$ TeV using the ALICE detector, (analysis note: https://aliceinfo.cern.ch/Notes/node/200), 2013.

[5] Rohlf, James William, Modern Physics from α to Z0, Chapter 1, Wiley, 1994.

[6] http://cds.cern.ch/record/516471/files/0109006.pdf

[7] http://aliceinfo.cern.ch/Public/en/Chapter1/results.html

[8] http://www.physics.umd.edu/courses/Phys741/xji/chapter2.pdf

[9] http://newstate-matter.web.cern.ch/newstate-matter/Experiments.html

[10] Eds. R.C. Hwa and X.-N. Wang, Quark-Gluon Plasma 4, World Scientific Publishing, 2010.

[11] http://www.phy.duke.edu/research/NPTheory/QGP/transport/index.php

[12] K. Yagi, T. Hatsuda, Y. Miake, Quark-Gluon Plasma: From Big Bang to Little Bang, Cambridge University Press, 2005.

[13] T. Matsui, H. Satz, J/ψ suppression by quark-gluon plasma formation, Physics Letters B, volume 178, number 4, 1986.

[14] R. Snellings, Elliptic Flow: A Brief Review, arXiv:1102.3010 [nucl-ex], 2011.

[15] STAR collaboration, C. Adler et al, Elliptic flow from two- and four-particle correlations in Au+Au collisions at RHIC, Phys. Rev. Lett. 97, 012301 (2006).

[16] W. Florkowski, Phenomenology of ultra-relativistic heavy ion collisions, World Scientific, 2010.

[17] STAR collaboration, Two-particle correlations with STAR, J. Phys.: Conf. Ser. 110 032003, (2008).

[18] http://www.star.bnl.gov/central/focus/highPt/

[19] A. Mischke, Overview on heavy flavour measurements in lead-lead collisions at the CERN-LHC, PoS ConfinementX 202 (2012).

[20] B. Muller, Nucl. Phys. A 750, 84 (2005).

[21] S. S. Adler et al., Phys. Rev. Lett. 94, 082301 (2005).

[22] Y. Zhang et al., J. Phys. G: Nucl. Part. Phys. 32, S529 (2006).

[23] Y. Dokshitzer and D. Kharzeev, Phys. Lett. B 519, 199 (2001).

[24] M. Djordjevic, M. Gyulassy and S. Wicks, Phys. Rev. Lett. 94, 112301 (2005).

[25] S. Wicks, W. Horowitz, M. Djordjevic and M. Gyulassy, Nucl. Phys. A 784, 426 (2007).

[26] MinJung Kweon for the ALICE Collaboration, Measurement of electrons from heavy-flavour decays in pp and Pb-Pb collisions, arXiv: 1208.5411v2 [nucl-ex], 2012.

[27] A. Grelli for the ALICE Collaboration, Heavy Flavour Physics with the ALICE detector at the CERN-LHC, J. Phys.: Conf. Ser. 316, 012025 (2011).

[28] Th. Bird, An Overview of the ALICE Experiment, School of Physics and Astronomy, University of Southampton, United Kingdom, 2010.

[29] R. S. de Rooij, Prompt D^{*+} production in proton-proton and lead-lead collisions, measured with the ALICE experiment at the CERN Large Hadron Collider, PhD thesis, Utrecht University, 2012.

[30] Harmonic decomposition of two particle angular correlations in Pb-Pb collisions at $\sqrt{s_{\rm NN}} = 2.76$ TeV, ALICE Collaboration, Physics Letters B 708 (2012) 249-264.

[31] Elliptic flow of electrons from Heavy-flavour hadron decays in Pb-Pb collisions at $\sqrt{s_{\rm NN}} = 2.76$ TeV (ALICE Analysis note), https://aliceinfo.cern.ch/Notes/node/92.

[32] ALICE Collaboration, Anisotropic flow of charged hadrons, pions and (anti-)protons measured at high transverse momentum in Pb-Pb collisions at $\sqrt{s_{\rm NN}} = 2.76$ TeV, Physics Letters B 719, 1828 (2013).

[33] A. Fantoni, The ALICE Electromagnetic Calorimeter: EMCAL, J. Phys.: Conf. Ser. 293, 012043 (2011).

[34] J. R. Taylor, An Introduction to Error Analysis: The Study of Uncertainties in Physical Measurements, 2nd edition, University Science Books, 1997.

[35] M. Paterno, Calculating Efficiencies and Their Uncertainties, Fermi National Accelerator Laboratory, 2003, http://home.fnal.gov/ paterno/images/effic.pdf.

[36] Azimuthal angular correlations of heavy flavour decay electrons and charged hadrons in proton-proton collisions at $\sqrt{s} = 7$ TeV using the ALICE detector (ALICE Analysis note), https://aliceinfo.cern.ch/Notes/node/198.

[37] K. Aamodt et al. (ALICE Collaboration), Particle-Yield Modification in Jetlike Azimuthal Dihadron Correlations in Pb-Pb Collisions at $\sqrt{s_{\rm NN}} = 2.76$ TeV, Phys. Rev. Lett. 108, 092301 (2012).

[38] M. Cacciari et al., JHEP 0103, 006 (2001) and private communication, 2012.

[39] ALICE EMCal Physics Performance Report, arXiv:1008.0413 [physics.ins-det], 2010.